CHARACTERIZATION OF IN-SITU STRESS AND PERMEABILITY IN FRACTURED RESERVOIRS

SEMI-ANNUAL TECHNICAL PROGRESS REPORT

for Period 22 May 2004–21 November 2004

by

Daniel R. Burns
and
M. Nafi Toksöz

Earth Resources Laboratory
Department of Earth, Atmospheric, and Planetary Sciences
Massachusetts Institute of Technology
Cambridge, MA 02139

February 4, 2005

Prepared for
THE U.S. DEPARTMENT OF ENERGY
AWARD NUMBER DE-FC26-02NT15346

This technical progress report was prepared with the support of the U.S. Department of Energy, under Award No. DE-FC26-02NT15346. However, any opinions, findings, conclusions, or recommendations expressed herein are those of the authors and do not necessarily reflect the views of the DOE.

DISCLAIMER

This report was prepared as an account of work sponsored by an agency of the United States Government. Neither the United States Government nor any agency thereof, nor any of their employees, makes any warranty, express or implied, or assumes any legal liability or responsibility for the accuracy, completeness, or usefulness of any information, apparatus, produce, or process disclosed, or represents that its use would not infringe privately owned rights. Reference herein to any specific commercial product, process, or service by trade name, trademark, manufacturer, or otherwise does not necessarily constitute or imply its endorsement, recommendation, or favoring by the United States Government or any agency thereof. The views and opinions of authors expressed herein do not necessarily state or reflect those of the United States Government or any agency thereof.

Abstract

Numerical modeling and field data tests are presented on the Transfer Function/Scattering Index Method for estimating fracture orientation and density in subsurface reservoirs from the 'coda' or scattered energy in the seismic trace. Azimuthal stacks indicate that scattered energy is enhanced along the fracture strike direction. A transfer function method is used to more effectively indicate fracture orientation. The transfer function method, which involves a comparison of the seismic signature above and below a reservoir interval, effectively eliminates overburden effects and acquisition imprints in the analysis. The transfer function signature is simplified into a scattering index attribute value that gives fracture orientation and spatial variations of the fracture density within a field.

The method is applied to two field data sets, a 3-D Ocean Bottom Cable (OBC) seismic data set from an offshore fractured carbonate reservoir in the Adriatic Sea and a 3-D seismic data set from an onshore fractured carbonate field in the Middle East. Scattering index values are computed in both fields at the reservoir level, and the results are compared to borehole breakout data and Formation MicroImager (FMI) logs in nearby wells. In both cases the scattering index results are in very good agreement with the well data. Field data tests and well validation will continue.

In the area of technology transfer, we have made presentations of our results to industry groups at MIT technical review meetings, international technical conferences, industry workshops, and numerous exploration and production company visits.

Report Contributors:

D. R. Burns
S. Chi
S. Grandi
B. Minsley
R. Rao
M. N. Toksoz
M. E. Willis
Y. Zhang

TABLE OF CONTENTS

I. Executive Summary

The purpose of this project is to develop and implement large-scale numerical models to quantify the effects of fracture parameter variations on seismic reflection signals and in-situ stress variations on flexural modes in boreholes. These models will be used as the basis of data analysis and inversion routines for estimating the heterogeneous fracture distribution in fractured reservoirs from seismic and borehole field data. Fracture property distributions estimated from seismic data will be used to estimate the permeability tensor in the reservoir for input to reservoir simulators.

In this period we continued work on numerical modeling and field data tests on the Transfer Function/Scattering Index Method for estimating fracture orientation and density in subsurface reservoirs from the 'coda' or scattered energy in the seismic trace. Modeling results indicate that in the direction normal to aligned fractures, forward and backscattered energy creates a complex wavefield that will not constructively interfere in the stacking process. In the direction parallel to the fractures there is only forward scattering present and the resulting wavefield can be enhanced in the stacking process. Laboratory physical modeling of acoustic scattering from a grooved surface (Schultz and Toksoz, 1995) shows similar behavior. Azimuthal stacking, therefore, will enhance the scattered energy along the fracture strike direction. A transfer function method is used to more effectively indicate fracture orientation. The transfer function method, which involves a comparison of the seismic signature above and below a reservoir interval, effectively eliminates overburden effects and acquisition imprints in the analysis. The transfer function signature is simplified into a scattering index attribute value that gives fracture orientation and spatial variations of the fracture density within a field.

The method is applied to two field data sets, a 3-D Ocean Bottom Cable (OBC) seismic data set from an offshore fractured carbonate reservoir in the Adriatic Sea and a 3-D seismic data set from an onshore, fractured carbonate field in the Middle East. Scattering index values are computed in both fields at the reservoir level, and the results are compared to borehole breakout data and Formation MicroImager (FMI) logs in nearby wells. In both cases the

scattering index results are in very good agreement with the well data. Initial tests on a third data set, from an onshore field in North America, have been undertaken. Although well data was not available for validation, the results are stable and suggest variations in the spatial distribution of fractures in the field.

Technology transfer efforts have been significant in the past eight months. Presentations of our results have been made to industry groups at MIT technical meetings, international technical conferences, industry workshops, and numerous exploration and production company visits.

II. Introduction

The purpose of this project is to develop and implement large-scale numerical models to quantify the effects of fracture parameter variations on seismic reflection signals and in-situ stress variations on flexural modes in boreholes. These forward modeling efforts will be used to develop data analysis and inversion routines for estimating the heterogeneous fracture distribution in fractured reservoir from seismic and borehole field data. These fracture property distributions will be used to estimate the permeability tensor in the reservoir by using statistical and discrete feature network techniques. Permeability estimates will then be used as inputs to reservoir simulators. The objective of the project is schematically displayed in Figure 1.

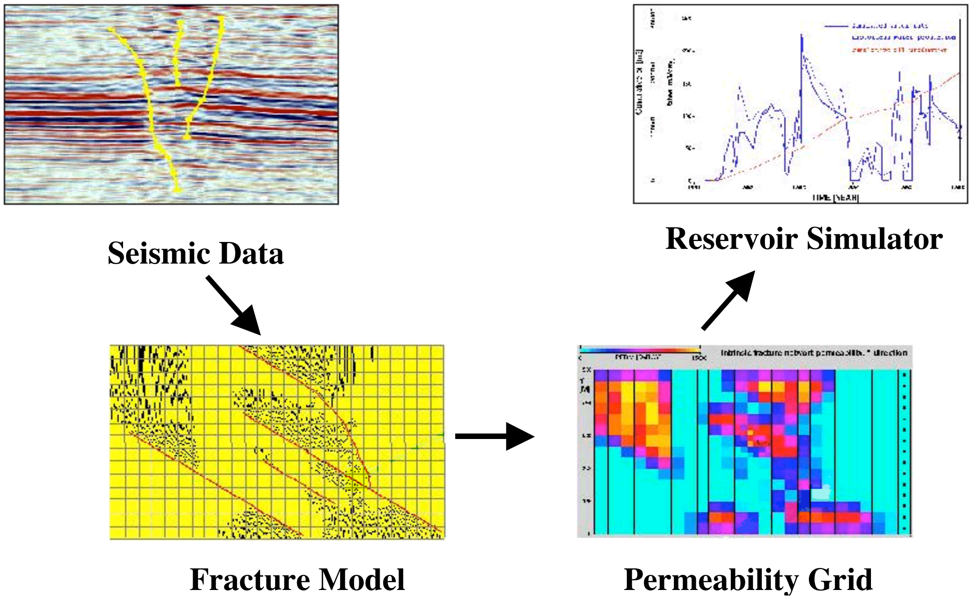

Figure 1. Schematic display of the project objectives. Surface 3-D seismic data is used to estimate the spatial distribution of fracture parameters (e.g., fracture density, spacing, orientation). A model is used to convert such fracture parameters into permeability values, which are input to reservoir simulators for history matching.

III. Results and Discussion

In our previous report we provided an overview of two new seismic analysis methods we developed for estimating fracture properties from the scattered wavefield: 1) spectral analysis of prestack scattered wave integrated amplitudes, and 2) the Transfer Function/Scattering Index method for reservoir interval analysis. The methods were tested on numerical modeling data and on field data from an offshore fractured carbonate reservoir (Willis et al., 2004a, b). We also tested an updated amplitude-variations-with-offset and azimuth (AVOA) method on the same field data (Minsley et al., 2004). In this report we provide additional numerical modeling test results on the transfer function/scattering index method and show test results from the offshore data set as well as a new onshore data set from a fractured carbonate reservoir.

A. Fracture properties from seismic data – lab and numerical modeling

We have been focusing most of our attention on the Transfer Function/Scattering Index method. This method analyzes the 'coda' or scattered energy in the seismic trace and relates this energy to the presence of fractures. Azimuthal variations in the resulting scattering index attribute are related to the orientation or strike of the fractures. As a brief review, we model a simple reservoir geometry consisting of five horizontal layers using the 3-D elastic finite difference code developed by Lawrence Berkeley National Laboratory (Nihei et al., 2002). All the layers except the third layer are homogeneous and isotropic elastic media. The third layer is 200-m thick and contains parallel, vertical fractures that are one grid cell thick (5m) and run the entire width of the model. The fractures are represented by equivalent anisotropic medium parameters using the method of Coates and Shoenberg (1995). Vlastos et al. (2003) use this same representation in a 2-D pseudospectral approach for modeling scattering from fractures. It should also be noted that the 5m grid cell width does not mean that the fractures themselves are that size, but that this 5m cell contains some number of fractures resulting in a more compliant fractured zone whose properties are represented by the equivalent medium properties given by the Coates and Shoenberg (1995) method. We generated a series of models with different fracture spacings (from 10m to 100m). We also generated a model with 'random' fracture spacing (i.e., a Gaussian distribution of spacings) and a model with two fracture sets (with different orientations and spacings). All models use a 40Hz Ricker wavelet as the seismic source (a compressional wavelength of 100m). The receiver spacing is 5m in both the inline and cross line directions. Details on these results can be found in previous reports, and a summary is given in Appendix A (Burns et al., 2004).

Figure 2 shows the shot records for the 50m fracture spacing case acquired in directions normal and parallel to the fractures. Scattered energy generated from the fractures dominates the shot records below the reservoir level (about 300 msec). It is clear on the shot record normal to the fracture direction that there is no coherent energy in or below the reservoir level, while for the parallel case, there are many coherent events that can be seen primarily below the base reservoir reflection on the shot record. In the direction parallel to the fractures, the seismic energy seems to be guided by the aligned fractures and the resulting scattered energy is more coherent and similar to the direct P wave reflection.

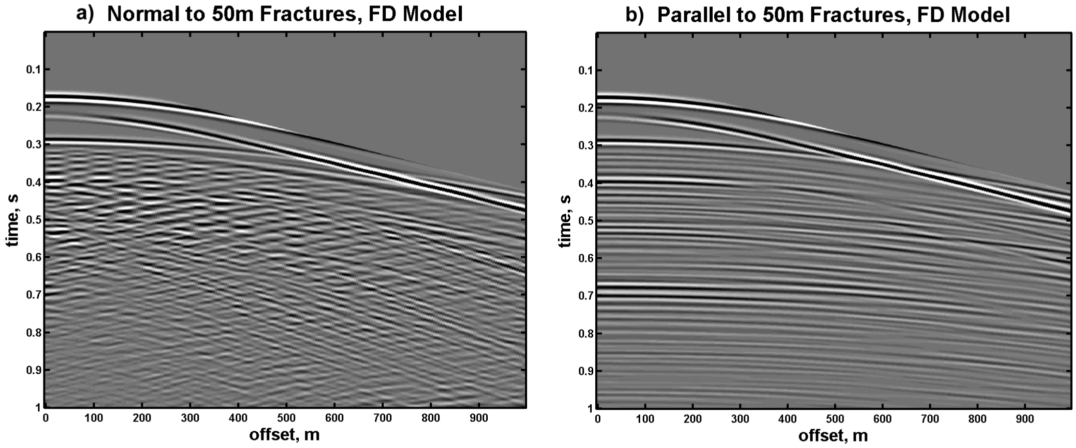

Figure 2. Vertical component of the 3D Finite difference modeling for 50m fracture spacing from Willis et al. (2004a, b): a) shows the shot record acquired normal to the fractures, b) shows the shot record acquired parallel to the fracture direction.

It is interesting to note that we have seen this same behavior of scattering for a different, but analogous problem in the laboratory. A series of laboratory ultrasonic measurements were made on models with rough surfaces (Schultz and Toksoz, 1995). In one set of experiments the scattered wavefield was measured in different directions relative to the orientation of a series of parallel grooves etched onto the surface of an aluminum block (Figure 3). Although this is not a fractured medium, it does provide a physical analogue to our problem. Schultz and Toksoz (1995) found that the scattered wavefield was different when measured normal to the grooves and parallel to the grooves. Normal to the grooves the combination of forward and back scattered energy creates a complex shot record (Figure 4), while the shot record parallel to the grooves contains only forward scattered energy (Figure 5). These observations are quite similar to what we see in the fractured model results (Figure 2). The numerical modeling of the grooved aluminum block (Figure 4 bottom panel) shows that this behavior is modeled very well with the finite difference technique that we are using for our fractured reservoir applications. These laboratory results provide a level of validation of our observations of scattering effects in our numerical modeling.

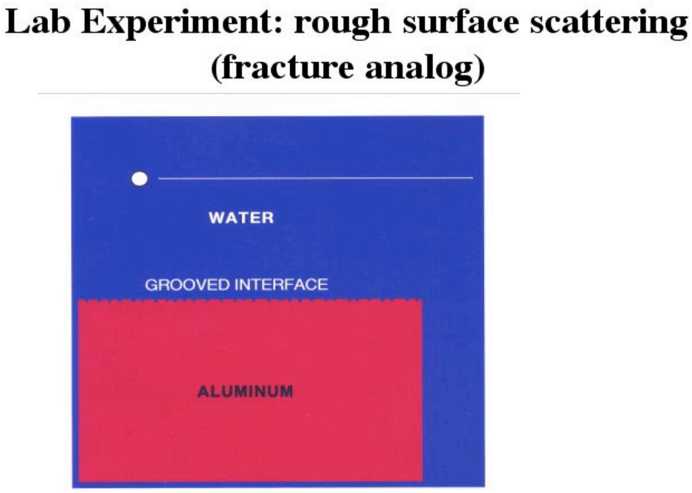
Lab Experiment: rough surface scattering (fracture analog)

Figure 3. Schematic of ultrasonic model for measurements of scattering from a grooved aluminum block. (After Schultz and Toksoz, 1995).

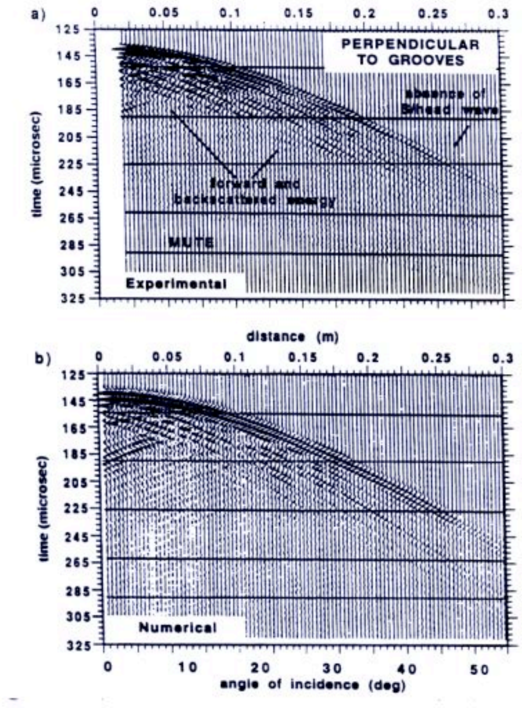

Lab data
(Normal to Grooves)

Finite Difference

Figure 4. Laboratory ultrasonic data acquired normal to the grooves (top panel), and finite difference calculations for the same model geometry (bottom panel). (After Schultz and Toksoz, 1995)

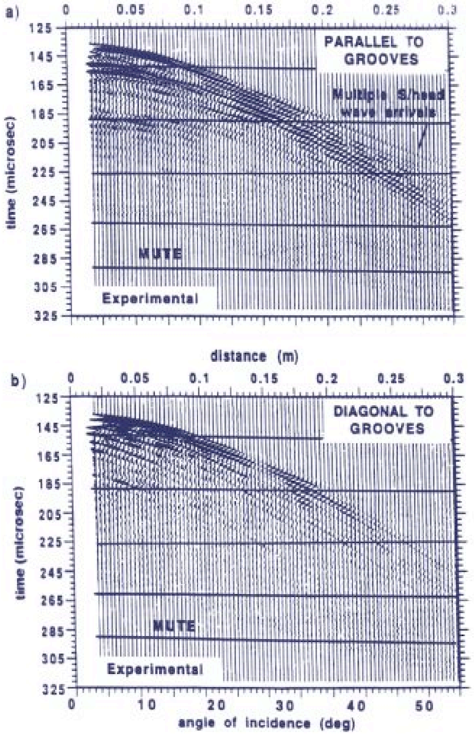

Lab data
(Parallel to Grooves)

Lab data
(Diagonal to Grooves)

Figure 5. Laboratory ultrasonic data acquired parallel to the grooves (top panel), and at an angle to the grooves (bottom panel). (After Schultz and Toksoz, 1995)

The pattern of azimuthal variations in the shot records seen in Figure 2 is observed for each of the different fracture spacing models that we generated. For shot records acquired normal to the fracture direction, the forward and back scattered diffraction-like events seen in Figure 2 do not stack together well with any Normal Moveout Velocity (NMO) velocity. For shot records acquired parallel to the fractures, however, much of the scattered energy will stack constructively. This azimuthal variation in stacking is the basis of the Transfer Function/Scattering Index method for fracture characterization. Figure 6 shows the full range of azimuthally stacked traces for the model with 50m fracture spacing (data shown in Figure 2). The top trace is the stacked trace for the shot record oriented parallel to the fractures, while the trace second from the bottom is the stacked trace for the shot record normal to the fractures (the two shot records in Figure 2 are shown for reference next to the appropriate stacked trace). The 'control' trace (the bottom trace in Figure 6) is the stacked trace for the case with no fractures. The other traces in the Figure are the result of stacking along 10° increments in azimuth. The stacked traces are quite similar until we get to the top trace, that is the azimuthal direction parallel to the fractures. For this trace the waveform is more complex, displaying a more 'ringy' character. This ringy character is the stacked 'coda' or scattered energy from the fractures. If we look at the azimuthal stack traces for the range of models that we generated (Figure 7a) we see that the behavior is extremely repeatable. That is, for all model cases the stacked trace parallel to the fractures is significantly different in character from all other azimuthal directions. The character of the azimuthally stacked traces, therefore, provides a measure of the orientation of fractures in the subsurface.

Azimuthal Stacks - Fracture Orientation

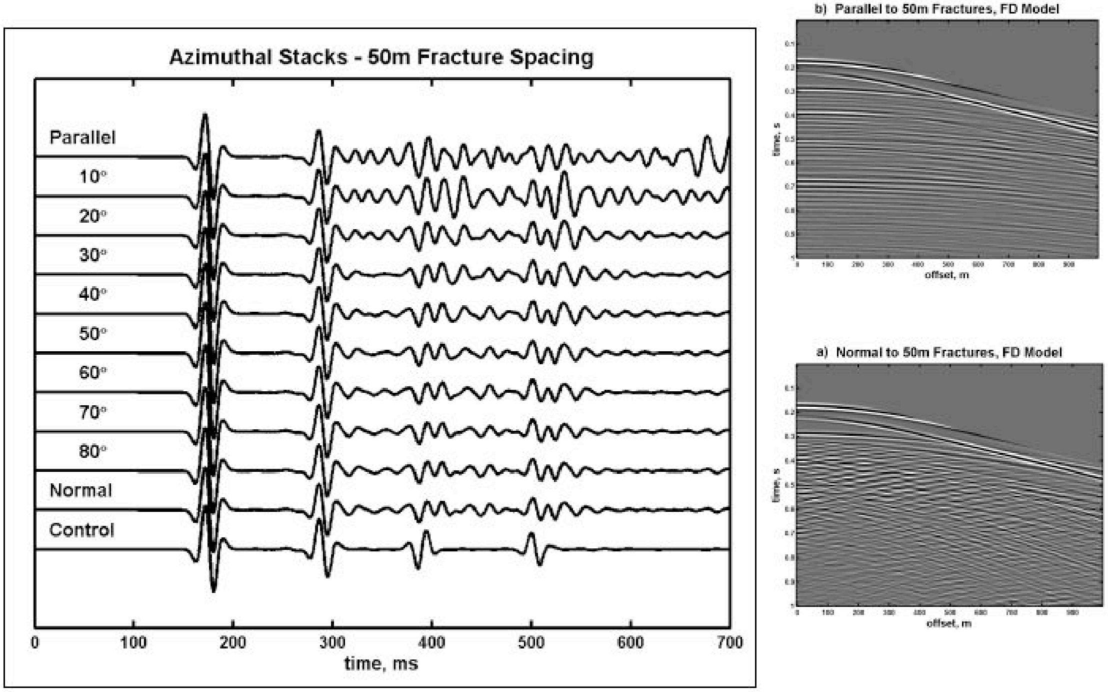

Figure 6: Stacked traces at 10° increments in azimuth from the 3D numerical model data. The lower most trace marked 'control' is the stacked trace for a model with no fractures. The trace labeled 'normal' is the stacked trace for a gather oriented normal (90°) to the fracture trend. The upper most trace labeled 'parallel' is the stacked trace oriented parallel to the fracture trend (i.e., along the fracture strike direction). On the right side of the figure the actual data gathers for normal (bottom) and parallel (top) to the fractures, as shown in Figure 2, are given next to their respective stacked traces.

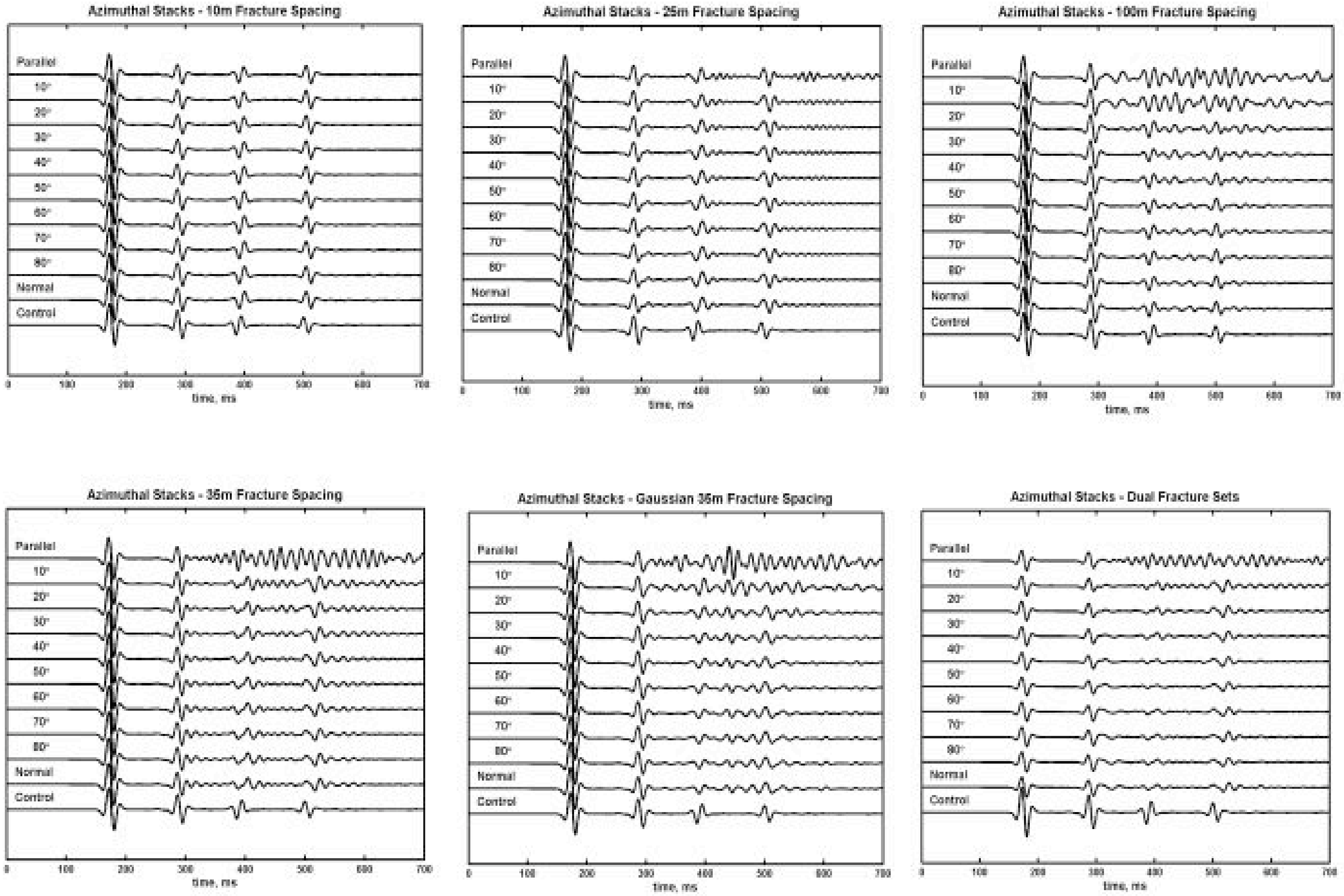

Figure 7a: Azimuthal stack traces for six different models (clockwise starting from the upper left: 10m fracture spacing, 25m fracture spacing, 100m fracture spacing, dual fracture set (35m spacing and 100m spacing oriented at 45°), Gaussian distribution of fracture spacing with a mean of 35m, and 35m fracture spacing). In each panel the bottom most trace is the 'control' (no fractures), the second from the bottom is 'normal' to the fractures, and the top trace is 'parallel' to the fractures. The intermediate traces are stacks at 10° increments in azimuth. Note that for all models the stacked trace oriented parallel to the fractures shows the most complex trace due to the scattered energy. The 10m model (top left) is below the resolution for these model parameters, and so no scattering effects are seen.

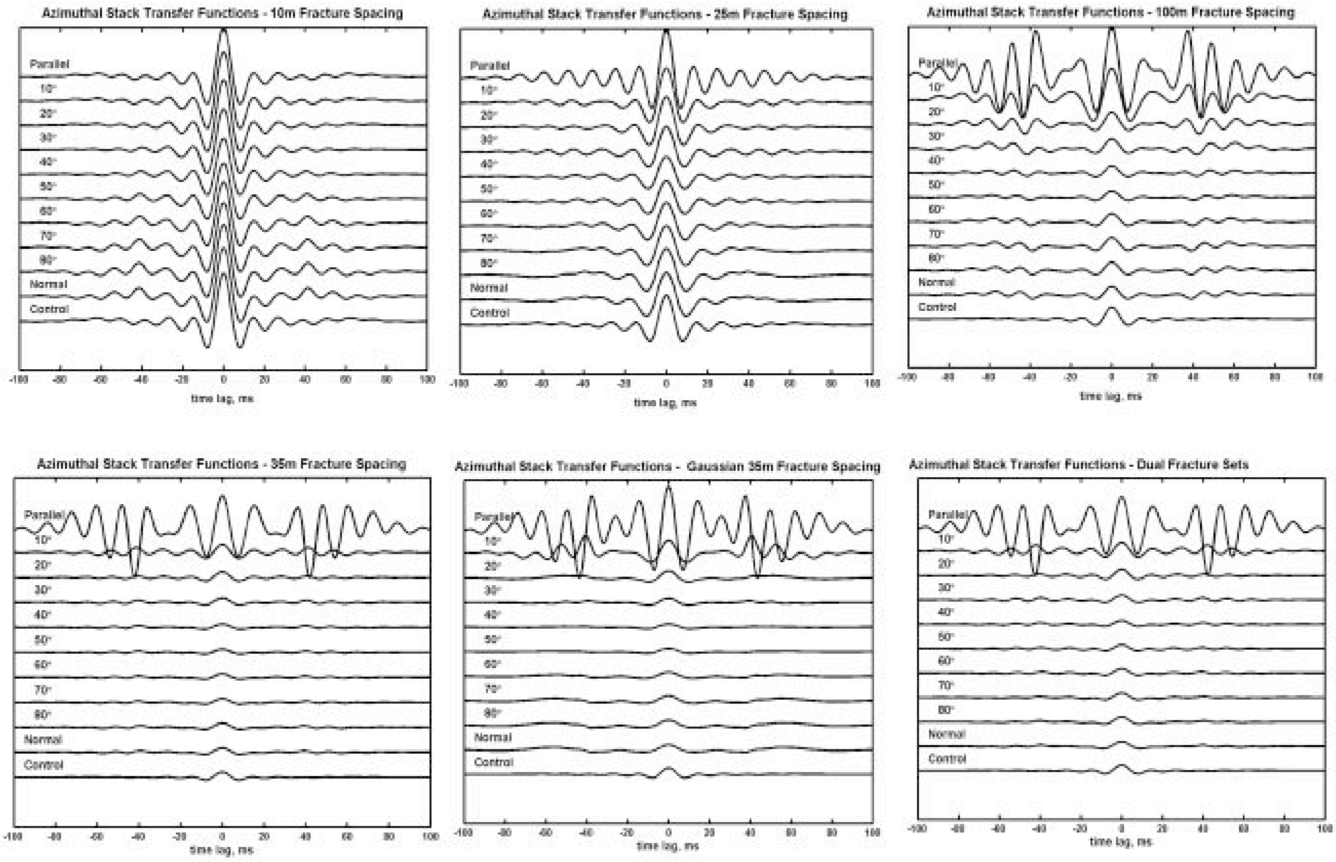
Azimuthal Stack Transfer Functions - 10m Fracture Spacing

Azimuthal Stack Transfer Functions - 25m Fracture Spacing

Azimuthal Stack Transfer Functions - 100m Fracture Spacing

Azimuthal Stack Transfer Functions - 35m Fracture Spacing

Azimuthal Stack Transfer Functions - Gaussian 35m Fracture Spacing

Azimuthal Stack Transfer Functions - Dual Fracture Sets

Figure 7b: Transfer functions corresponding to the azimuthal stack traces shown in Figure 7a. The transfer function shows large amounts of 'ringiness', or large amplitude values at late lag values for the traces stacked parallel to the fractures. For the 10m spacing case, the model behaves as an equivalent medium because the spacing is below the seismic resolution for this model. The 25m spacing (middle top panel) is very close to the resolution limit for these model parameters, so there is only minor ringiness in the transfer function.

The approach we take to quantify the changing character of the azimuthal stacked traces is referred to as the Transfer Function/Scattering Index Method. For the simple models shown in Figure 7a it is relatively easy to see that the scattering effects begin below the second reflector (that is, the top of the fractured reservoir interval) on traces parallel to the fracture direction. However, in field data we expect to have a much more difficult time observing these scattered wavetrains due to the nearly continuous nature of the subsurface reflectivity. In addition, if there are fractured zones or other scatterers in the overburden, those scattered waves will contaminate, or overprint, the scattered energy from our zone of interest in the reservoir. To address these complications we start with concepts from existing methods of seismic wavelet estimation to obtain two apparent (or temporally local) source wavelets from the reflection time series – one from above the fractured zone (the "input" wavelet) and one below it (the "output" wavelet). These wavelets are represented by their autocorrelations obtained from windowed portions of the reflection time series above and below the fractured zone of interest (Willis et al., 2004a, 2004b).

We then compute the time domain transfer function between the autocorrelations of the two extracted wavelets. The transfer function is computed by deconvolving the autocorrelation of the input wavelet from the autocorrelation of the output wavelet. This transfer function characterizes the effect of scattering in the interval of interest, between the two windowed portions of the trace. A simple pulse shaped transfer function indicates no scattering, while a long ringing transfer function captures the scattering within the reservoir interval. It should be especially noted that any contamination from scattering above the interval will be present in both the input and output extracted wavelets and thus will be excluded from the transfer function. Therefore, this method removes overburden effects from the analysis, a very important aspect of any reservoir analysis technique.

By applying this method to data stacked in different azimuthal directions, the interval transfer function should exhibit greater ringing in the direction parallel to fracturing. Figure 7b shows the transfer functions derived for the models of different fracture spacings whose stacked traces are shown in Figure 7a. Clearly evident on the transfer function for the parallel direction is its ringiness away from the zero lag while in the normal direction the transfer function is comparatively compact. In all cases, the transfer function shows significant energy at non-zero lag values parallel to the fracture direction and quite compact transfer functions at all other azimuthal directions.

In order to quantify the amount of transfer function ringiness we compute a Scattering Index, SI, defined by:

$$SI = \sum_{i=0}^{m} | t_i | i^n$$

where i is the time lag, t_i is the transfer function (time domain) amplitude at lag i, n is an exponent, typically equal to unity, and m is a lag at which there is no more significant energy in the transfer function. The more the transfer function rings, the larger the value of the Scattering Index. If the transfer function is a simple spike (i.e. representing no scattering) then the Scattering Index attains a value of zero.

If we compute the Scattering Index for the transfer function at each azimuth for several of the models, the result is shown in Figure 8 (note: the computations are made for the first quadrant of the figure and the results replicated for the other three quadrants). This figure shows the strong directionality of the scattering index attribute for all fracture spacing cases. When the fracture spacing is small relative to the dominant wavelengths (e.g., the 25m case, which is 1/4 wavelength of the compressional wave in this model) the effect is small. Interestingly the maximum effect for this set of examples seems to correspond to a tuning effect for fracture spacing of 35m (which is about 1/2 the shear wavelength in this model).

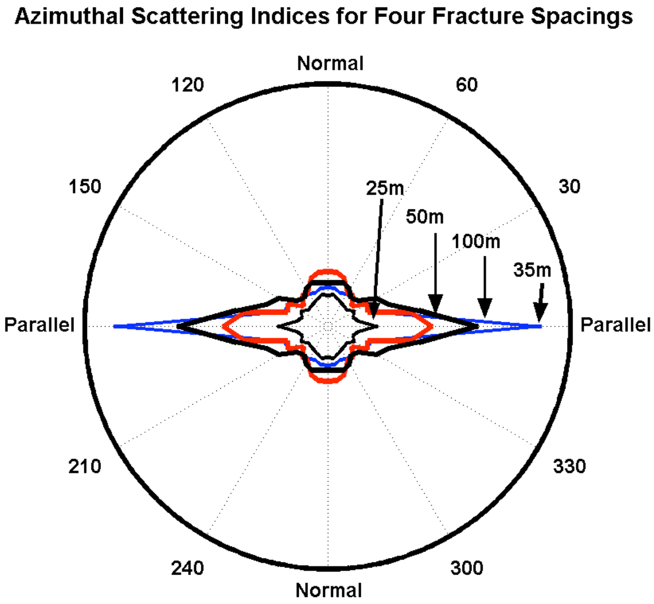

Figure 8: Scattering Index values plotted as a function of azimuth. These values were derived from the transfer functions for the numerical modeling data for different fracture spacings. For all fracture spacings the scattering index is maximum in the direction parallel to the fractures. The variations in the magnitude of the scattering index are a function of the fracture spacing relative to the source wavelength. In this example there is a tuning effect for the 35m case resulting in a maximum signature in the scattering index.

B. Fracture properties from seismic data – field data tests

We are testing our Scattering Index method on several data sets. The first is a 3-D Ocean Bottom Cable (OBC) multicomponent seismic data set from an offshore fractured carbonate reservoir in the Adriatic Sea. These data, along with well log, core, and production information, were provided by ENI Agip. The second is a 3-D seismic data set from an onshore, fractured carbonate field in the Middle East. These data, together with production data and a number of Formation MicroImager (FMI) logs, were provided by Shell Oil Company. Previous studies on both fields have resulted in a well-characterized understanding of the fracture network, which together with FMI and other well information provides us with a benchmark for validating our results. We have also obtained limited access to a third data set from an onshore field in the Canadian foothills. The availability of data from several different fields with different acquisition parameters provides opportunities for more thorough testing of our methods. In this section we summarize our current results on these data, including initial validation using well information.

B.1: Data Set 1 - Emilio Field (offshore OBC data)

The Emilio Field is a fractured carbonate reservoir located in the Adriatic Sea in about 80m of water. The field is an area of complex folding and faulting at a depth of approximately 2800m. A high quality 3D/4C seismic survey was acquired using ocean bottom cables (OBC). The acquisition parameters were selected to insure excellent azimuthal coverage of the area, making the data ideal for the testing of our methods (Figure 9). Borehole studies suggest the presence of two orthogonal fracture sets oriented ENE and NNW (Angerer et al, 2002). Other studies have also investigated this 3D seismic data using PP and PS wave anisotropy to identify fracture characteristics of the reservoir level (Vetri et al, 2003; Gaiser et al, 2001).

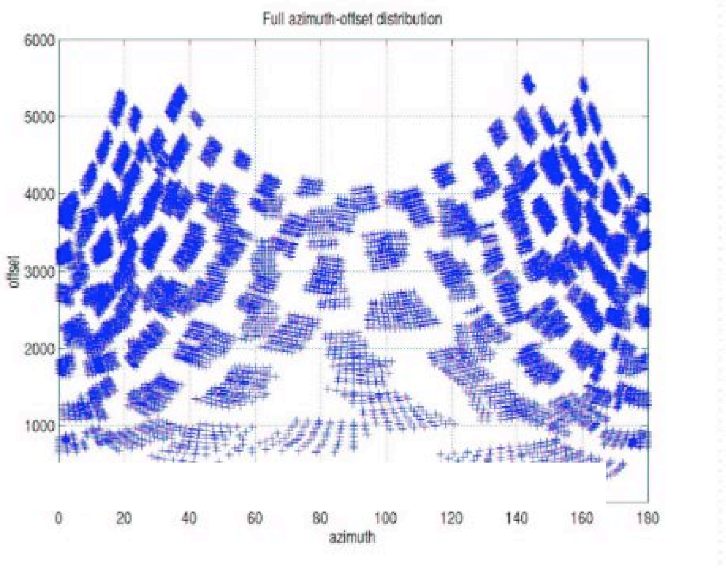

Figure 9: Offset-azimuth distribution for all traces that fall within an 8 x 8 super-CMP bin

Figure 9: Subsurface coverage of the OBC data as a function of azimuth and offset.

A stacked section showing the data and the reservoir interval used in our analysis is shown in Figure 10. The near to mid range offsets at each subsurface location of the preprocessed PP data (Vetri et al, 2003) were stacked in eighteen different azimuthal orientations from East to West using 20 degree wide overlapping ranges. This process created eighteen 3D stacked volumes. An example of the azimuthal stacks for one superbin location is shown in Figure 11. The transfer functions and scattering indices for the reservoir zone were computed for each of these stacked volumes at each subsurface location. An example polar plot of the scattering index values for one of the CDP locations in the field is shown in Figure 12. This polar plot can be compared to the similar plot for the numerical modeling data shown in Figure 8.

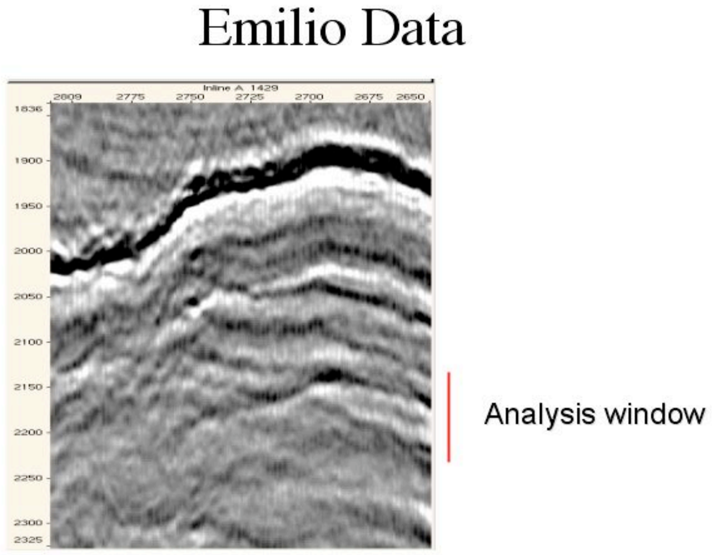

Figure 10: Stacked section from the 3D OBC data showing the analysis interval at the reservoir level.

The scattering indices were sorted and directions for those with the highest ranges of values are plotted in Figure 13, giving a map view of the location and direction of possible fractures determined by this method. Figure 14 shows histogrammed rose plots of the fracture distributions corresponding to the sixteen boxes outlined (by dashed lines) in Figure 13. In several boxes there appears to be no preferred orientation while in many of the boxes the ENE and NNW directions are strongly evident.

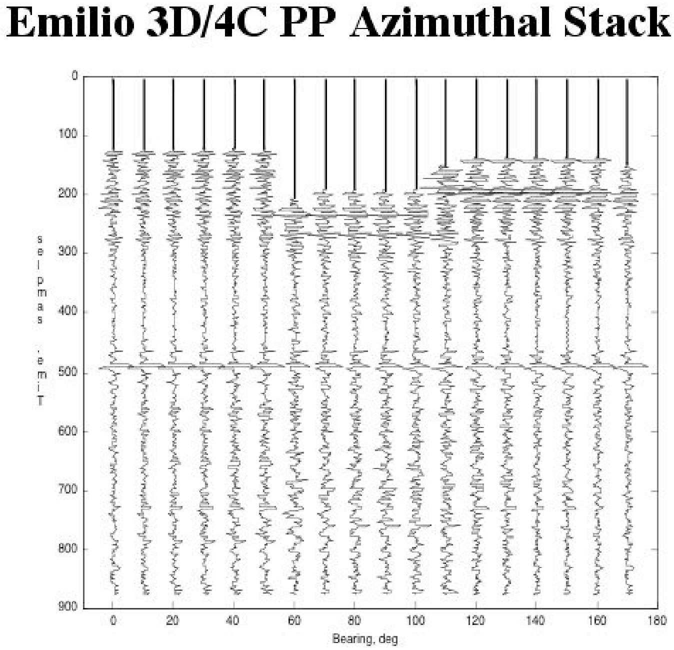

Figure 11: Azimuthal stack traces for one superbin location in the data. Data were stacked in 18 azimuthal directions. The reservoir interval is located below the marker horizon seen at time sample 500.

To validate our results we compare the fracture orientation histograms in Figure 14 to similar figures obtained from well log measurements at several wells in the field. In making such a comparison we must keep in mind that we are comparing results generated from a seismic analyses over a large area of the field (in this case 1/16 of the entire field area) to measurements made in a single well within that area. We are continuing to work on other approaches for appropriately comparing results of measurements made at very different scales. With this caveat in mind, Figure 15 shows three comparisons between the seismic Scattering Index results and well log measurements (FMI logs and borehole breakout measurements). The results are in excellent agreement with the well information at Wells 4 and 8. In Well 7 the FMI analysis identified the fractures as drilling induced rather than naturally occurring. These drilling induced fractures are local phenomena aligned in a NW-SE direction, while the seismic analysis suggests the natural fractures in the area as being aligned in a NE-SW direction. These drilling induced fractures are oriented with the maximum stress direction of the local stress field at the well location, while the fracture orientations derived from seismic scattering are a function of the stress field over a larger area of the field. It should also be noted that both the local drilling induced fractures and the larger scale seismic fracture estimates are oriented in directions consistent with the two principle fracture sets in the field. We will investigate the effectiveness of creating the histogram rose plots (e.g., Figure 14) for different subsurface area sizes (spatial scales) for comparisons with individual wells.

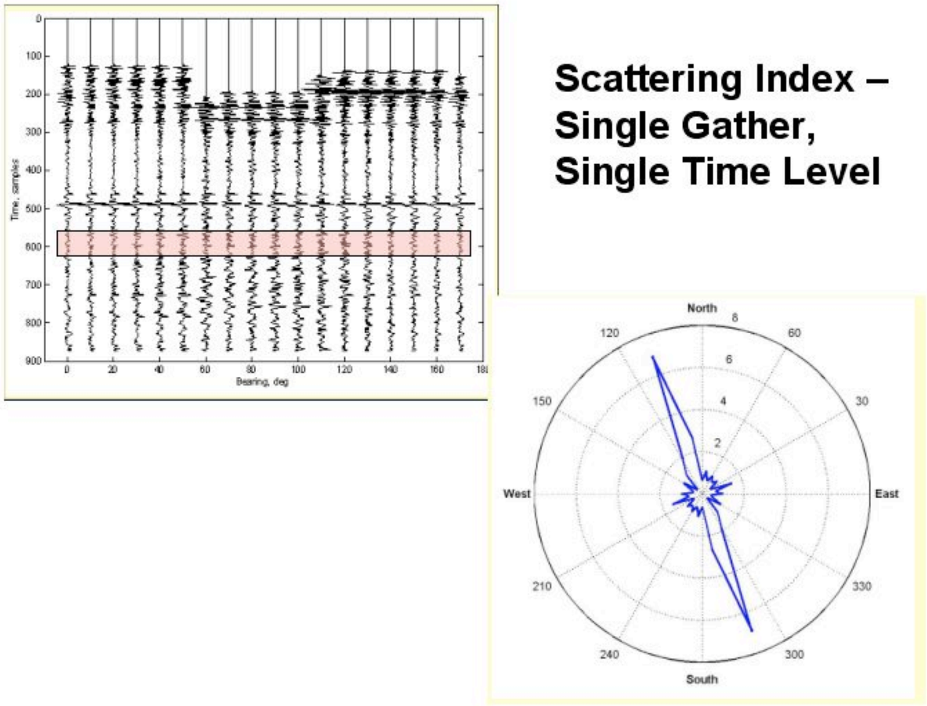

Figure 12. Polar plot of the azimuthal variation of scattering indices derived from the transfer functions at one CDP in the field data. The scattering index is largest in the direction parallel to the fracture orientation. This example is from one of the largest scattering index values (shown as black bars in Figure 13).

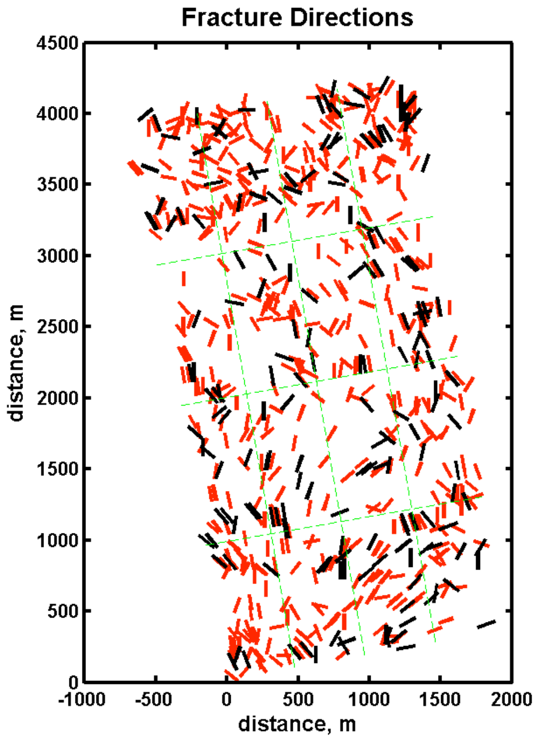

Figure 13. Scattering index quiver plots of the spatial orientation and distribution of fractures over the field. The black and red bars show the orientations for the top two bins of highest scattering indices. The dashed-line grid shows the location of the histogram plots in Figure 14.

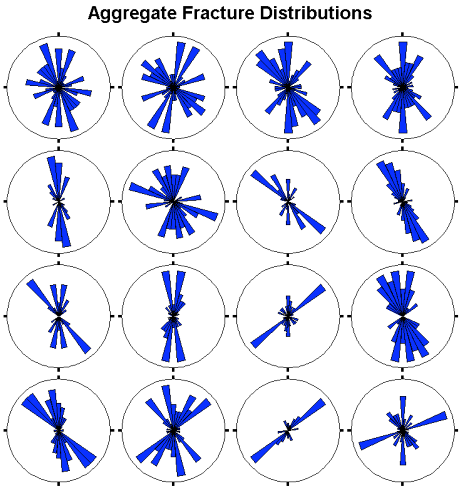

Figure 14. Angular histogram plots of the fracture distributions shown in Figure 13. Each plot represents the corresponding subportion of the field delineated by the dashed lines in Figure 13. The top of each plot represents fractures aligned North.

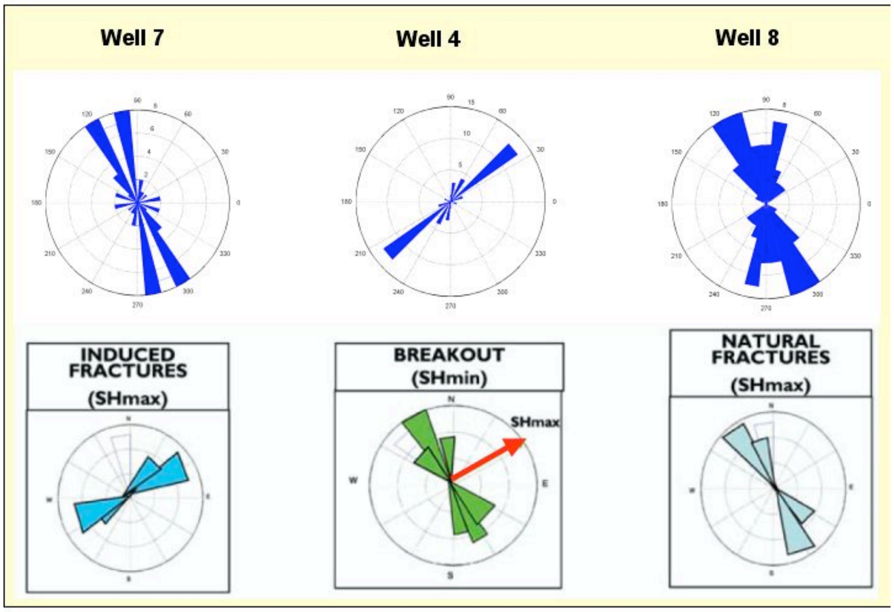

Figure 15: Comparison of scattering index rose plots (top three panels) with FMI and borehole breakout measurements at three different well locations in the field. The agreement is excellent for Wells 4 and 7. At Well 7 the FMI was responding to drilling induced fractures, which are a very local phenomenon related to the maximum horizontal stress at the location. Although the direction of these induced fractures is along one of the major fracture directions (e.g., as seen in Well 4), the seismic scattering index response for a larger spatial region surrounding that well indicates that the natural fractures are primarily aligned to the NW.

B.1: Data Set 2 – Onshore Fractured Carbonate Field

The second data set used for testing our method is from an onshore location in the Middle East. The field produces from a gently folded, shallow, fractured carbonate. Production is primarily controlled by fractures oriented in two directions: approximately N50°E (the most important system for fluid flow) and N40°W. The NE fractures occur in swarms separated by about 100-250m, interspersed with faults with the same orientation occurring every 500 to 1000m. The NW fractures also occur in swarms, but are spaced at distances of about 1000m. Figure 16 shows a map view of the field with structural contours of the reservoir and major faults (note the fault orientations). The black box outlines the seismic survey area, while the smaller grey box through the center of the field outlines the data that we have analyzed for this report. Figure 17 shows the fold distribution for the data as a function of azimuth and offset. As is often the case with onshore data acquisition, full fold coverage over a wide range of azimuths is not usually obtained. These data were collected with the receiver lines oriented N40°W (azimuth of 130° measured from due East), and the source points located in a zig-zag pattern between receiver lines. The result is a high CDP fold in the direction of the receiver lines, and lesser fold at other azimuths. Because our method uses data over all azimuth directions, and we want to keep the fold fairly consistent to avoid any directional bias, we limited our analysis to near offsets (to about 800 m). These constraints still resulted in reasonable fold coverage (approximately 100 fold). Figure 18 shows the resulting azimuthal stack traces for one CDP location. The analysis zone, covering the reservoir interval, is noted in red.

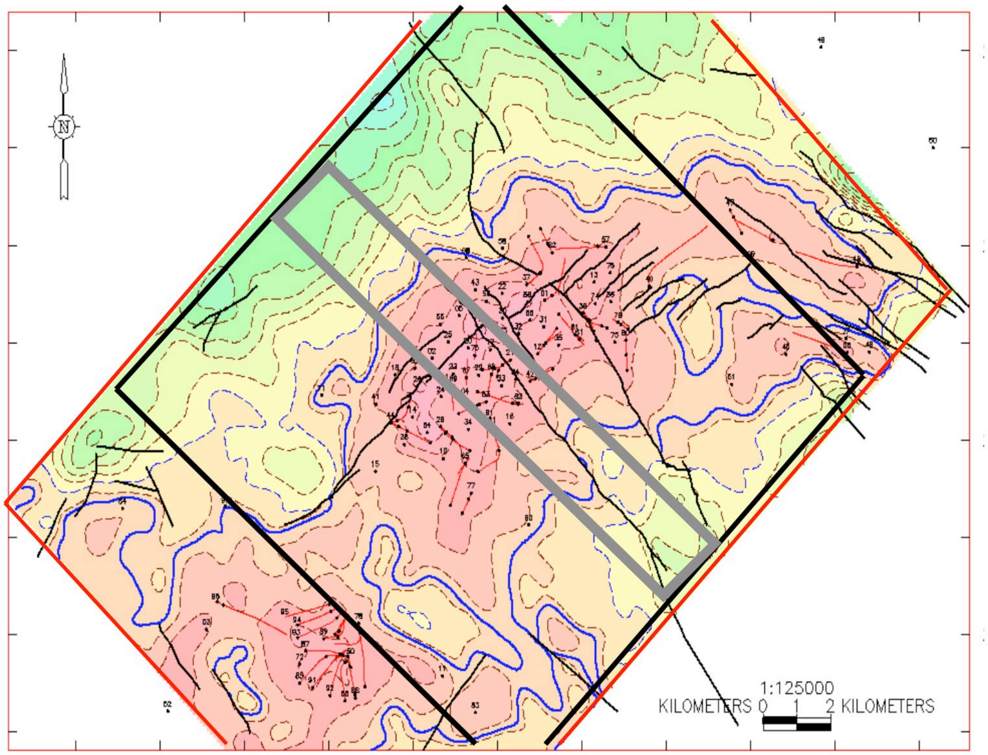

Figure 16: Map of data set 2 survey area (black box) over a fractured carbonate field in the Middle East. Two fault systems (striking NE/SW and NW/SE) are also shown. The grey rectangular box in the center of the field indicates the data swath of our initial analyses presented in this report.

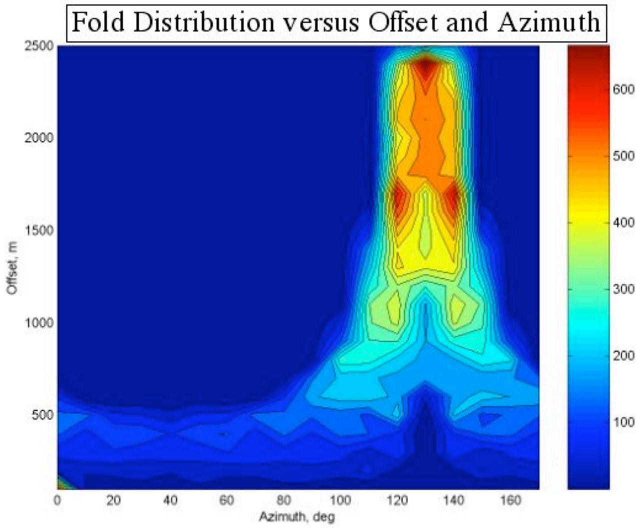

Figure 17: Fold distribution for data set 2 as a function of source-receiver azimuth and offset. For our analyses we used only near offset data (offset range of 0 – 800m) to maintain approximately constant fold for all azimuths.

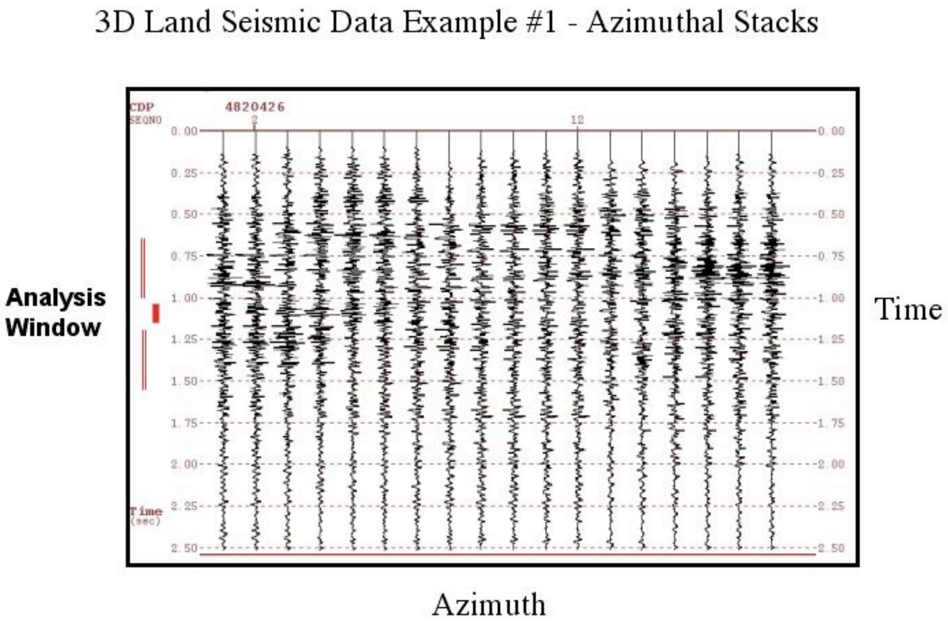

Figure 18: Azimuthal stack traces (10° increments) for data set 2. The analysis window for the transfer function calculation is shown in red on the left side of the figure (straddling the reservoir interval).

Following the same methodology used for the Emilio Field analysis, the Scattering Index was computed at each CDP location at the reservoir interval and the highest values are shown in Figure 19. We see two zones with high fracture density and the fracture orientations are predominantly aligned in the NE/SW and NW/SE directions. Figure 20 shows the same information in a histogram form (the analysis zone was separated into 8 blocks with each histogram representing the orientations of all the scattering index segments shown in figure19 within each box). The two dominant fracture orientations are more clearly evident in this figure. Figure 21 shows the distribution of wells with FMI logs in the study area. A comparison between the scattering index results and available FMI data from several nearby wells is shown in Figure 22. The FMI results show the histogram of the orientation for all identified fractures in the logged interval. These initial comparisons show good general agreement between our seismic scattering method and measured FMI data from nearby wells.

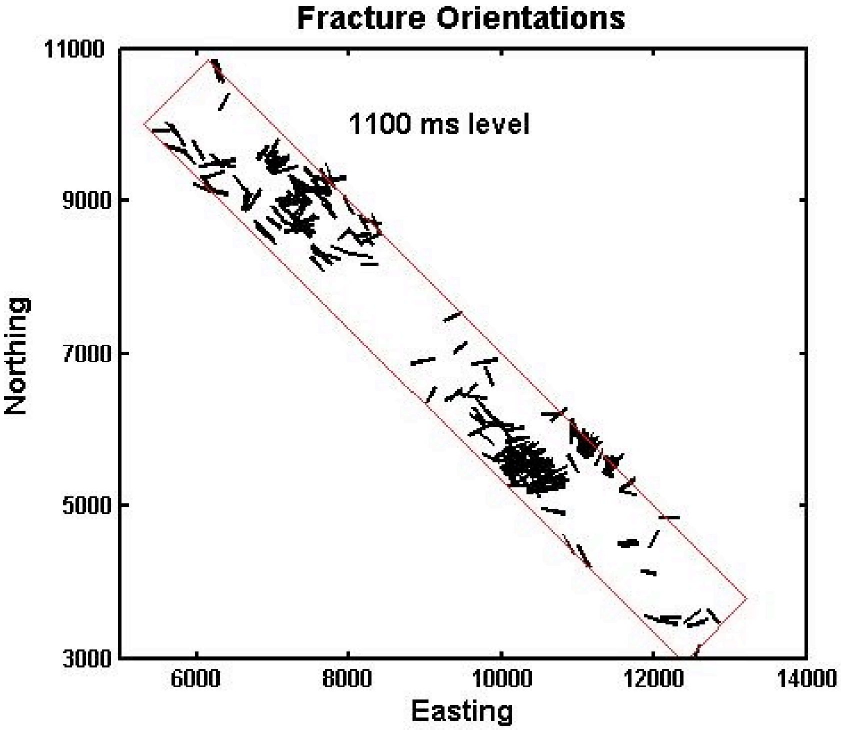

Figure 19**:** Scattering index quiver plot showing the spatial orientation and distribution of fractures over the analyzed area in data set 2. The bars show the orientations for the top two bins of highest scattering indices.

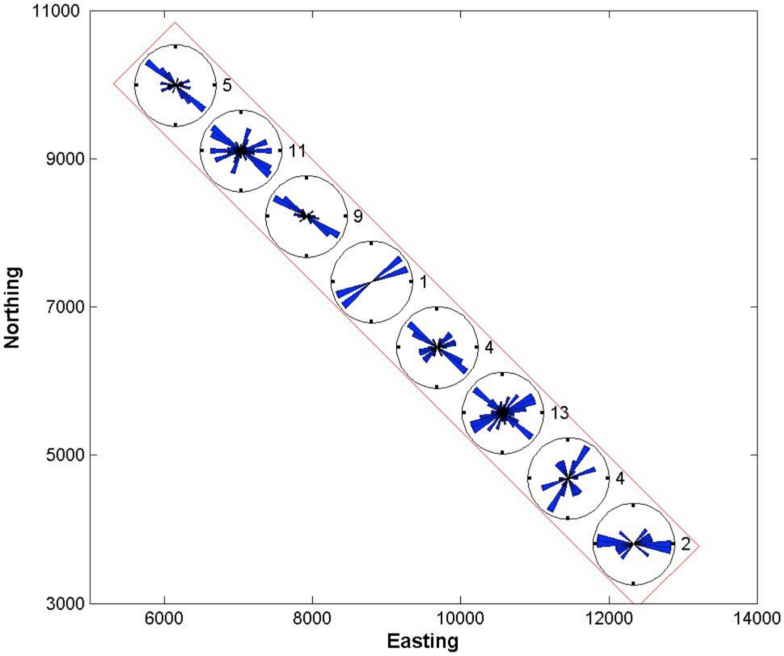

Figure 20: Angular histogram plots of the fracture distributions shown in Figure 19. Each plot represents the corresponding subportion of the field in Figure 19. The top of each plot represents fractures aligned North.

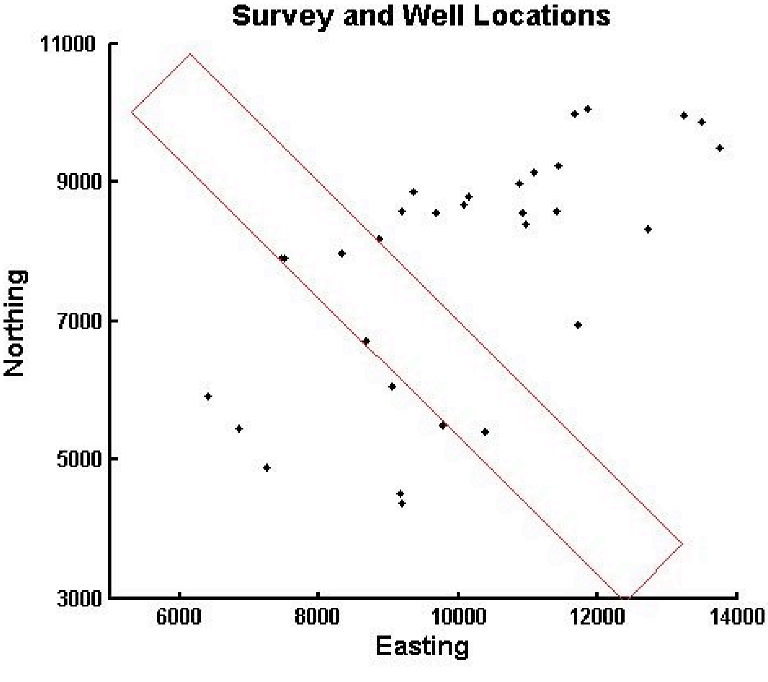

Figure 21: Plot of the analyzed area of data set 2 (red box) showing the location of available wells with FMI fracture orientation data (black diamonds).

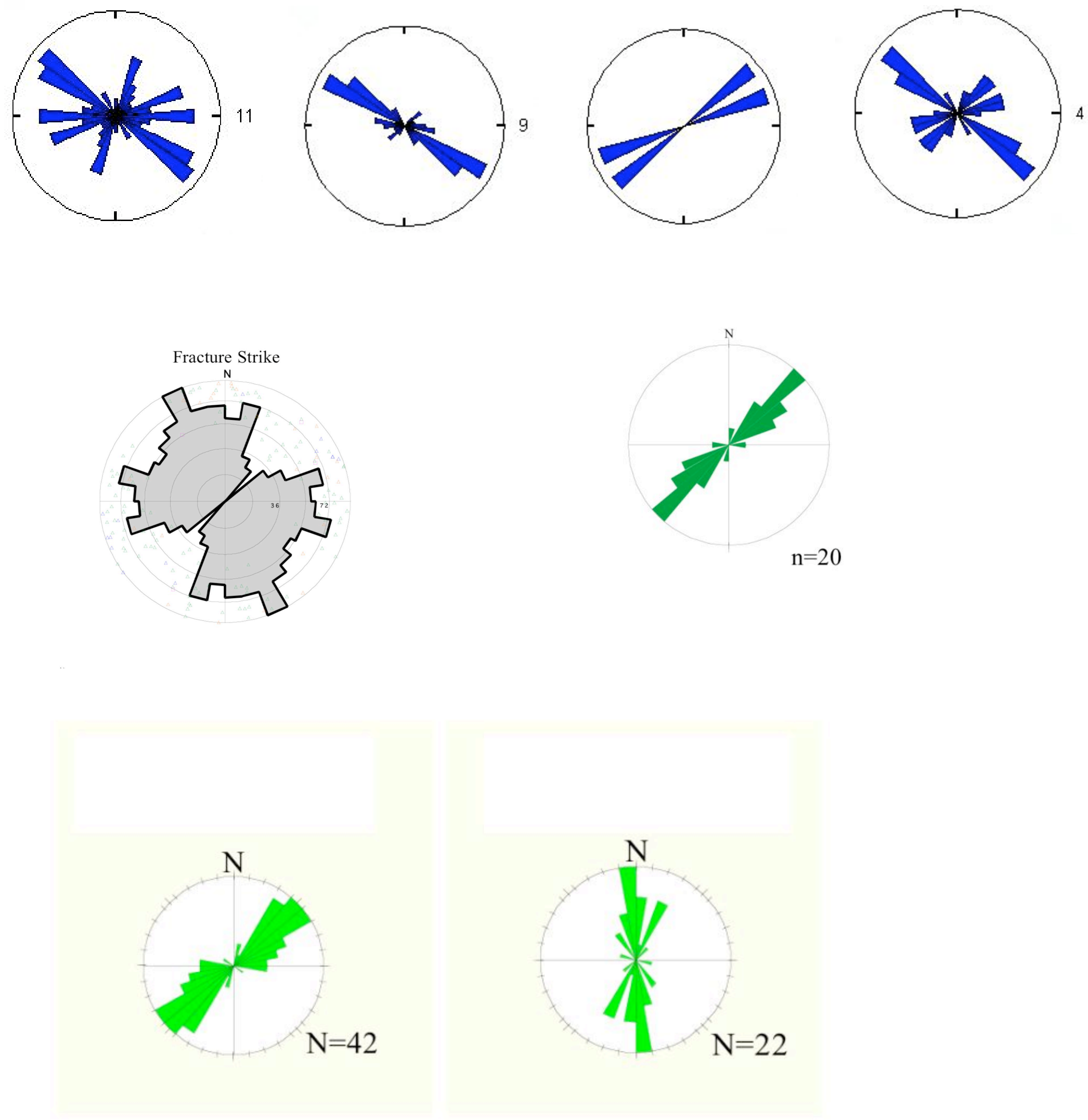

Figure 22: Angular histogram (rose) plots generated from the seismic scattering index analysis in the central portion of our study area (top 4 panels) with example FMI data from several wells in the same area (bottom 4 panels)

B.2: Data Set 3 – Onshore Fractured Carbonate Field

The Scattering Index method was also tested on a second onshore data set from a fractured carbonate field in Canada. The results show interesting spatial variations in the fracture distribution in the field. Although no supporting information was made available, this test provided some confirmation that the analysis method is stable and can be applied to 3D data sets in North America.

C. Fracture permeability estimation – flow modeling

Work continues on numerical and statistical approaches to permeability estimation. As described in previous reports, the Oda-model statistical approach (Oda, 1985; Brown and Bruhn, 1998) provides a promising link from the seismic scattering index analysis to a permeability tensor estimate with appropriate calibration at wells for aperture and length distributions.

D. Borehole dispersion analysis and stress estimation

Integrated borehole methods, including the inversion of cross-dipole flexural mode dispersion curve cross over (e.g., Huang, 2003) provides a useful set of tools for estimating in-situ stress variations. The Appendix B contains a preprint of a paper on this topic (Grandi, 2004).

IV. Technology Transfer

During the past several months we have made presentations of our results to industry groups at the Earth Resources Laboratory annual technical meeting, three international conferences, two industry workshops, and numerous company visits. Our annual industry consortium meeting (held in May, 2004) was attended by representatives from ten exploration and production, and oilfield services companies. Presentations were made at the International EAGE meeting (June, 2004 in Paris), the SEG meeting

(October, 2004 in Denver), the SEG-Japan meeting (November, 2004 in Sendai, Japan), and at two industry workshops (the SEG Summer Workshop on Fractured Reservoirs held in Vancouver in August 2004, and the ConocoPhillips research workshop on Fractured Reservoirs held in Calgary in October 2004). Finally, presentations were also made to individual company research and production groups in Houston and Denver over the past eight months.

V. Conclusions

The Scattering Index method has been tested on the three field data sets, one offshore OBC data set and two land data sets. Comparison of our results with FMI well data suggests that our methods are able to provide information on fracture orientation and spatial variations in fracture density within a reservoir. We are continuing to work on methods to extract additional information from the scattered wave amplitudes and spectral characteristics. Work is also continuing on using the seismic analysis results to calculate estimates of fracture permeability by means of the Oda model.

V. References

Angerer, E., Horne, S., Gaiser, J., Walters, R., Bagala, S., 2002, Characterization of dipping fractures using Ps mode-converted data, *SEG Expanded Abstracts*.

Brown, S.R. and Bruhn, R.L., 1998, Fluid permeability of deformable fracture networks, *J. Geophys. Res., 103*, 2489-2500.

Burns, D. R., Willis, M. E., Minsley, B. J., and Toksoz, M. N., 2004, Characterizing Subsurface Fractures from Reflected and Scattered Seismic Energy, Proceedings SEG Japan Meeting, Sendai, Japan.

Coates, R.T. and Shoenberg, M., 1995, Finite difference modeling of faults and fractures, *Geophysics*, **60**, 1514-1526.

Gaiser, J., Loinger, E., Lynn, H, and Vetri, L, 2002, Birefringence analysis at the Emilio field for fracture characterization, *First Break* v 20, 505-514.

Grandi, S., 2004, In-situ stress field from breakouts and flexural wave crossovers and comparison with plate tectonic models, preprint.

Huang, X, Sinha, B., Burns, D., Toksoz, M. N., 1999, Formation stress estimation using standard acoustic logging, *69th Ann. Int. Mtg. Soc. Expl. Geophys. Expanded Abstracts*, 53-56.

Minsley, B., Willis, M., Krasovec, M., Burns, D., and Toksoz, M.N., 2004, Fracture detection using amplitude versus offset and azimuth analysis of a 3D P-wave seismic dataset and synthetic examples, *74th Annual SEG Meeting, Expanded Abstracts*.

Nihei, K.T., et al., 2002, Finite difference modeling of seismic wave interactions with discrete, finite length fractures, *72nd Ann. Int. Mtg. Soc. Expl. Geophys. Expanded Abstracts*.

Oda, M., 1985, Permeability tensor for discontinuous rock masses, *Geotechnique, 35*, 483-495.

Schultz, C. and Toksoz, M. N., 1995, Reflections from a randomly grooved interface: ultrasonic modeling and finite difference calculations, *Geophys. Prospecting*, *43*, 581-594.

Vetri, L., Loinger, E. Gaiser, J. Grandi, A., Lynn, H, 2003, 3D/4C Emilio: Azimuth processing and anisotropy analysis in a fractured carbonate reservoir, *The Leading Edge*, 675-679.

Vlastos, S., Liu, E., Main, I.G., Li, X.Y., Numerical simulation of wave propagation in media with discrete distributions of fractures: effects of fracture sizes and spatial distributions, *Geophys. J. Int.*, **152**, 649-668.

Willis, M.E., Pearce, F, Burns, D.R, Byun, J. and Minsley, B, 2004a, Reservoir fracture orientation and density from reflected and scattered seismic energy, *EAGE meeting Paris*.

Willis, M., Rao, R., Burns, D., Byun, J., Vetri, L., 2004b, Spatial orientation and distribution of reservoir fractures from scattered seismic energy, *74th Annual SEG Meeting, Expanded Abstracts*.

Characterizing Subsurface Fractures from Reflected and Scattered Seismic Energy

Daniel R. Burns[(1)], Mark E. Willis[(1)], Burke J. Minsley[(1)], and M. Nafi Toksoz[(1)]
[(1)]*Earth Resources Laboratory, Department of Earth, Atmospheric, and Planetary Sciences, Massachusetts Institute of Technology, Cambridge, MA USA (burns@mit.edu)*

ABSTRACT

Two new methods have been developed for estimating fracture orientation and density in subsurface reservoirs from scattered wavefield signals. In the first, fracture density is estimated from the wavenumber spectra of the integrated amplitudes of the scattered waves as a function of offset in pre-stack data. The second method is based upon observations, from 3D finite difference modeling, that regularly spaced, discrete vertical fractures impart a ringing coda-type signature to any seismic energy that is transmitted through or reflected off of them. This coda energy is greatest when the acquisition direction is parallel to the fractures, the seismic wavelengths are tuned to the fracture spacing, and when the fractures have low stiffness. The method uses surface seismic reflection traces to derive a transfer function, which quantifies the change in an apparent source wavelet propagating through a fractured interval. The transfer function for an interval with low scattering will be more spike-like and temporally compact. The transfer function for an interval with high scattering will ring and be less temporally compact. When a 3D survey is acquired with a full range of azimuths, the variation in the derived transfer functions allows the identification of subsurface areas with high fracturing and the orientation (or strike) of those fractures. The method was calibrated with model data and then applied to Ocean Bottom Cable (OBC) field data from a fractured reservoir giving results that agree with known field measurements. An amplitude versus offset and azimuth (AVOA) inversion method was applied to the same data and the fracture location and strike orientation estimates correlate with borehole information from the area.

KEY WORDS: fractured reservoirs, seismic scattering, AVOA, fracture parameter estimation, OBC data

INTRODUCTION

The way in which fractures in rock formations affect the seismic waves propagating through them depends on the fractures' mechanical parameters, such as compliance and saturating fluid, and on their geometric properties, such as dimensions and spacing. If the fractures and fracture spacing are small relative to the seismic wavelength, then the fractures cause the reservoir rock to behave like an equivalent anisotropic medium with a symmetry axis normal to the strike of the 'open' fractures. Resulting seismic reflections from the top and bottom of a fractured reservoir will display amplitude variations with offset and azimuth (AVOA) (e.g., Lynn et al., 1996). If the fractures and fracture spacing are close in size to the seismic wavelength, then the fractures will scatter the seismic energy causing a complex seismic signature or coda. This seismic signature will vary as a function of the orientation of the seismic acquisition relative to the fracture orientation. The scattered seismic energy not only provides information about the fracture orientation, but can also be analyzed to provide information about the fracture spacing and fracture density. Observations by previous researchers have demonstrated that scattering effects are sensitive to fracture density in field data as well as numerical and laboratory experiments (e.g., Ata and Michelena, 1995). In this paper we present two new methods to estimate fracture orientation and density from scattered waves in seismic data: spectral characteristics of scattered wavefields in pre-stack data, and a transfer function method for characterizing the scattered wavefield in post-stack data. We test both methods on numerical model data, and then apply the transfer function and AVOA methods to field data from an offshore fractured reservoir.

SEISMIC SCATTERING ANALYSIS - MODELING

Using the 3-D elastic finite difference code developed by Lawrence Berkeley National Laboratory (Nihei et al., 2002) we model a simple reservoir geometry consisting of five horizontal layers. All the layers except the third layer, are homogeneous and isotropic elastic media. The third layer is 200-m thick and contains parallel, vertical fractures which are as tall as the layer, one grid cell thick (5m) and run the entire width of the model. The fractures are represented by equivalent anisotropic medium parameters using the method of Coates and Shoenberg (1995). Vlastos et al. (2003) use this same representation in a 2-D pseudospectral approach for modeling scattering from fractures. We generated a series of models with the following fracture spacings: no fractures, 10m, 25m, 35m, 50m, 100m, and a Gaussian distribution of fracture spacings with a mean of 35m and a standard deviation of 10m. We created another model with two fracture sets, the primary set at 35m spacing aligned in the y direction and the secondary set, having a higher stiffness value, at 100m spacing aligned at 45 degrees to the first set. All models use a 40Hz Ricker wavelet as the seismic source. The receiver spacing is 5m in both the inline and cross line directions.

On the left side of Figure 1 are the shot records for the 50m fracture spacing case acquired in directions normal and parallel to the fractures. To the right of each shot record is its velocity analysis. Scattered energy generated from the fractures dominates the shot records below the reservoir level (about 300 msec). It is clear on the shot record normal to the fracture direction that there is no coherent stackable energy in or below the reservoir level. However, for the parallel case, there are many coherent events that can be seen primarily below the base reservoir reflection on the shot record and observed on the velocity analysis. In the direction parallel to the fractures, the seismic energy seems to be guided by the aligned fractures and the resulting scattered energy is more coherent and similar to the direct P wave reflection. This same pattern of azimuthal variation in the modeled scattered wavefields is observed for all the model results. For shot records acquired normal to the fracture direction, the disruptive forward and back scattered, diffraction-like events seen in Figure 1 do not stack together well with any NMO velocity. For shot records acquired parallel to the fractures, however, much of the scattered energy will stack constructively.

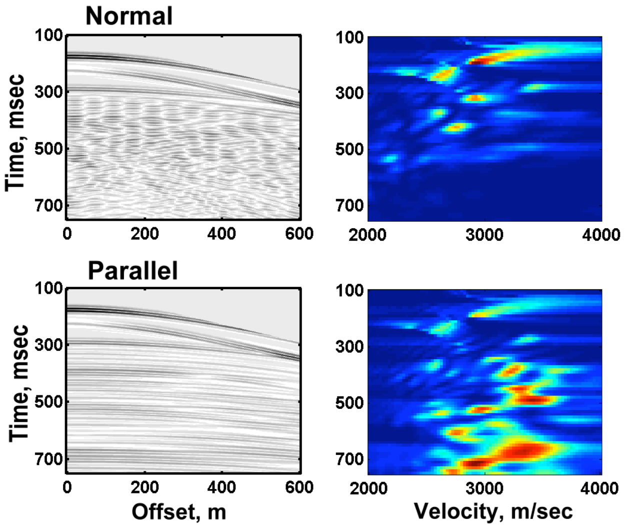

Figure 1. Left two plots show the seismic shot records for the model with 50m fracture spacing. The top left plot show the shot record normal to fractures, left bottom plot shows the shot record parallel to the fractures. The right two plots show the velocity spectra for the corresponding shot records on the left.

INTEGRATED AMPLITUDE METHOD

Our first method of analyzing the scattered wavefield signatures involves pre-stack data. Close inspection of the shot records acquired normal to the fracture direction reveals a beating or resonance phenomenon. The pattern of beating is different for each of the fracture spacing cases, and is most prominent on the near to middle offset range of traces. To study this, we computed the integrated absolute value of the amplitudes for each trace in a given shot record in an offset and velocity controlled time window through the scattered energy. The far offset traces were omitted from the analysis. The integrated amplitudes will be affected by the AVO response of the top and bottom reflection of the reservoir. However, this effect will be a predominantly long wavelength term on the integrated amplitudes versus offset. The approximate effect of the AVO term is removed by subtracting the best fit linear trend with offset from the integrated amplitudes prior to spectral analysis.

The top panel of Figure 2 shows synthetic shot record normal to the fractures for the 50m fracture spacing case. The scattered wavefield is windowed and the absolute value of the amplitude for each trace is summed within that window. The integrated trace amplitude versus offset is shown for the near and mid-offset traces. The analysis window followed the NMO velocity of the reservoir. The bottom panel of Figure 2 shows the wavenumber amplitude spectrum computed from the fast Fourier transform of these detrended amplitudes. Clearly visible in the wavenumber spectrum is a peak at 0.02/m, which corresponds to the fracture spacing of 50m. The same analysis was done on the other fracture spacing cases. Spectral peaks correctly identified the 100m, 50m and 35m fracture spacings, however due to the combination of source frequency content, receiver spacing and reservoir velocity, the 25m and 10m spacing cases were not resolvable. For the model of a Gaussian distribution of fractures with a mean spacing of 50m, a broader spectral peak was still present 0.02/m.

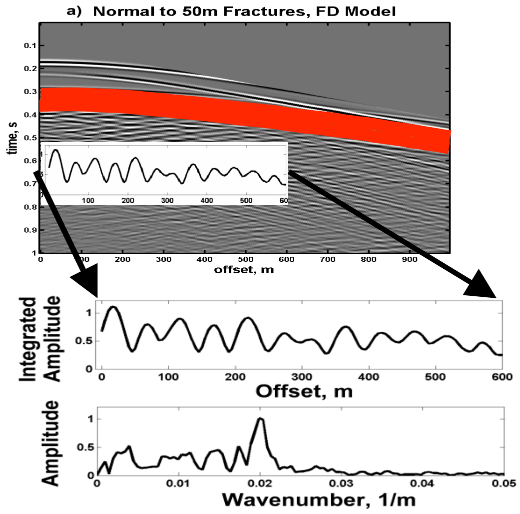

Figure 2. Top panel shows the synthetic shot record normal to the fractures at 50m spacing. The highlighted zone is the window for the integrated amplitude analysis. The middle panel shows the integrated amplitude versus offset and lower panel the corresponding wavenumber spectrum with a peak at 0.02/m (50m spacing).

TRANSFER FUNCTION METHOD

The second method of estimating fracture parameters from scattered wavefield data focuses on post-stack data. Figure 3 shows the results of applying NMO and stacking the model traces in different azimuthal directions. The trace labeled “normal” corresponds to the stack of the traces in the top left plot of Figure 1. The trace labeled “parallel” corresponds to the stack of traces in the bottom left plot of Figure 1. In between these two traces are those stacked traces corresponding to 10 degree increments between normal and parallel directions to the fractures. (For comparison, the bottom trace labeled “control” is the trace from the model with no fractures.) For shot records acquired normal to the fracture direction, the scattered wavefield does not stack together well with any NMO velocity and the final stacked trace is similar to the control trace. However, the scattered wave energy does stack in the direction parallel to the fractures. From these observations, the strike of the fracturing may be determined by identifying the azimuthal acquisition direction with shot records containing coherent, ringing energy which are enhanced the most when stacked.

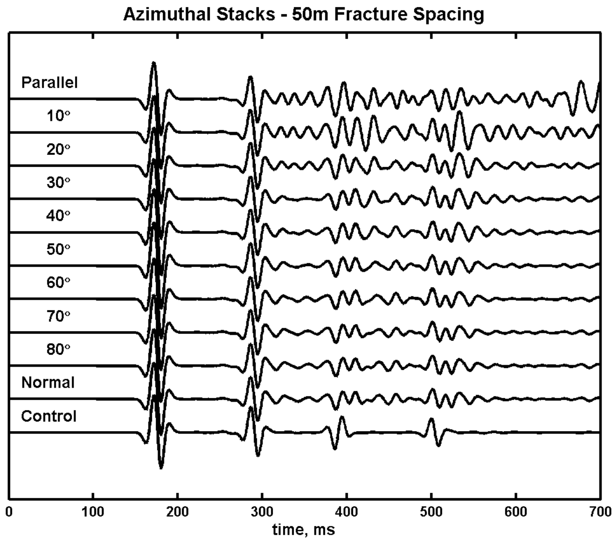

Figure 3. Plot showing the azimuthal stacks of traces from the 50m fracture spacing model. The traces represent azimuth stacks starting in the direction parallel to fracturing (top), and then increasing in 10 degree increments until normal to the fractures. The bottom trace shows the stack for the model without a fractured layer.

In the model data we generated, it might be possible to directly measure the scattered wavefield from the isolated reflectors in the reservoir zone. However, in field data we expect to have a more difficult time observing these scattered wavetrains due to the nearly continuous nature of the subsurface reflectivity. In addition, if there are fractured zones or other scatterers in the overburden, those scattered waves will contaminate, or overprint, the scattered energy from our zone of interest in the reservoir. So we start with the concepts from existing methods of seismic wavelet estimation to obtain two apparent (or temporally local) source wavelets from the reflection time series – one from above the fractured zone (the “input” wavelet) and one below it (the “output” wavelet). These wavelets are represented by their autocorrelations obtained from windowed portions of the reflection time series above and below the fractured zone of interest.

We then compute the time domain transfer function between the autocorrelations of the two extracted wavelets. The transfer function is computed by deconvolving the autocorrelation of the input wavelet from the autocorrelation of the output wavelet. This transfer function characterizes the effect of scattering in the interval of interest, between the two windowed portions of the trace. A simple pulse shaped transfer function indicates no scattering, while a long ringing transfer function captures the scattering within the reservoir interval. Notice that any contamination from scattering above the interval will be present in both the input and output extracted wavelets and thus will be excluded from the transfer function.

This method can be used on both pre-stack and post-stacked data. If it is applied to data stacked in different azimuthal directions, the interval transfer function should exhibit greater ringing in the direction parallel to fracturing. Figure 4 shows the transfer functions derived for the stacked traces in Figure 3. Clearly evident on the transfer function for the parallel direction is its ringiness away from the zero lag while in the normal direction the transfer function is comparatively compact. Similar results were found for each of the fracture models, including the Gaussian distribution of fracture spacings, as seen in Figure 5. For the model with two fracture sets at different orientations, the primary fracture set dominates the results, while the secondary fracture set (having higher stiffness values) has minimal effect. The transfer functions for this example look very similar to the results in Figure 5.

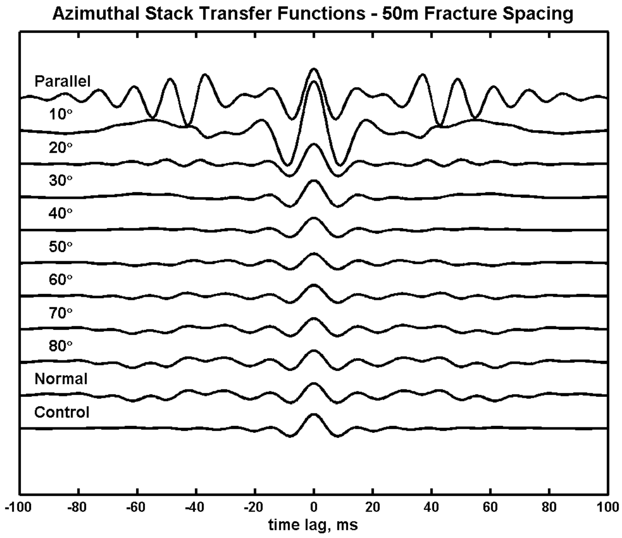

Figure 4. Plot showing the transfer functions corresponding to azimuthal stacks of traces (in Fig. 3) from the 50m fracture spacing model. The transfer functions correspond to azimuth starting in the direction parallel to fracturing (top), and then increasing in 10 degree increments until normal to the fractures. The bottom trace shows the transfer function for the model without a fractured layer.

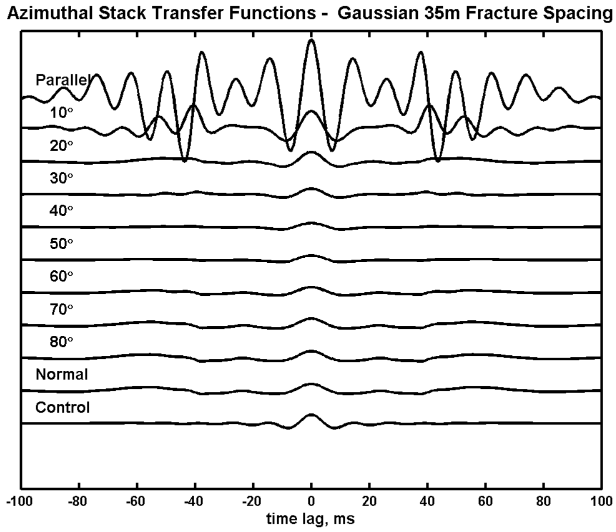

Figure 5. Plot showing the transfer functions corresponding to azimuthal stacks of traces for a model with a Gaussian distribution of fracture spacings (mean spacing of 35m and standard deviation of 10m). Even for non-uniform fracture spacing the transfer function displays high values at non-zero lag only in the direction parallel to the fractures.

In order to quantify the amount of transfer function ringiness or non-compactness, we created a scattering index, SI, defined by:

$$SI = \sum_{i=0}^{m} | t_i | i^n$$

where i is the time lag, t_i is the transfer function (time domain) amplitude at lag i, n is an exponent, typically equal to unity, and m is a lag at which there is no more significant energy in the transfer function. (It is also possible to normalize the scattering index based upon its energy and interval time sample or other such criteria.) The more the transfer function rings, the larger the value of the scattering index. If the transfer function is a simple spike, i.e. representing no scattering, then the scattering index attains a value of zero.

Figure 6 shows the scattering index values for models run with 25, 35, 50 and 100m fracture spacings. These results show that there is a clear maximum of the scattering index in the parallel direction. It is also clear that in the non-parallel directions the scattering index is not zero but fluctuates about a smaller, but fairly consistent value.

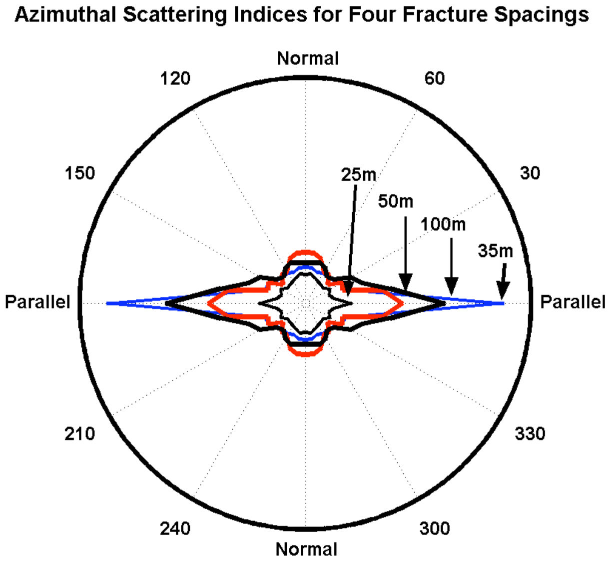

Figure 6. Polar plot of the azimuthal variation of scattering indices derived from the transfer functions of the 25, 35, 50 and 100m fracture spacing models. The scattering index is largest in the direction parallel to the fracture orientation. The largest scattering index is for the 35m fracture spacing, while the smallest shown is for the 25m spacing.

APPLICATION TO FIELD DATA

We applied the transfer function and AVOA methods to a 3D/4C seismic survey acquired over an offshore fractured carbonate reservoir in the Adriatic Sea. Borehole studies suggest the presence of two orthogonal fracture sets oriented ENE and NNW (Angerer et al, 2002). Recent studies have investigated this 3D seismic data using PP and PS wave anisotropy to identify fracture characteristics of the reservoir level (Vetri et al, 2003; Gaiser et al, 2001).

The near to mid range offsets of the preprocessed PP data (Vetri et al, 2003) were stacked in eighteen different azimuthal orientations from East to West using 20 degree wide overlapping ranges. This process created eighteen 3D stacked volumes. The transfer functions and scattering indices for the formation zone were computed for each of these stacked volumes. An example polar plot of the scattering index values for one of the CDP locations in the field is shown in Figure 7. The scattering indices were sorted and directions for those with the highest ranges of values are plotted in Figure 8, giving a map view of the location and direction of possible fractures determined by this method. Figure 9 shows histogrammed rose plots of the fracture distributions corresponding to the sixteen boxes outlined (dashed lines) in Figure 8. In several boxes there appears to be no preferred orientation while in many of the boxes the ENE and NNW directions are strongly evident. The results are consistent with borehole data from several wells in the field.

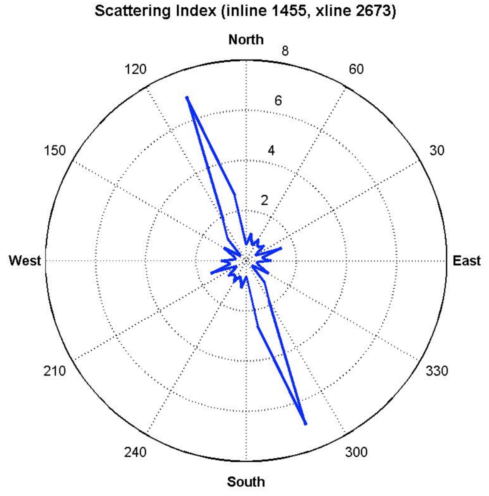

Figure 7. Polar plot of the azimuthal variation of scattering indices derived from the transfer functions at one CDP in the field data. The scattering index is largest in the direction parallel to the fracture orientation. This example is from one of the largest scattering index values (shown as black bars in Figure 8).

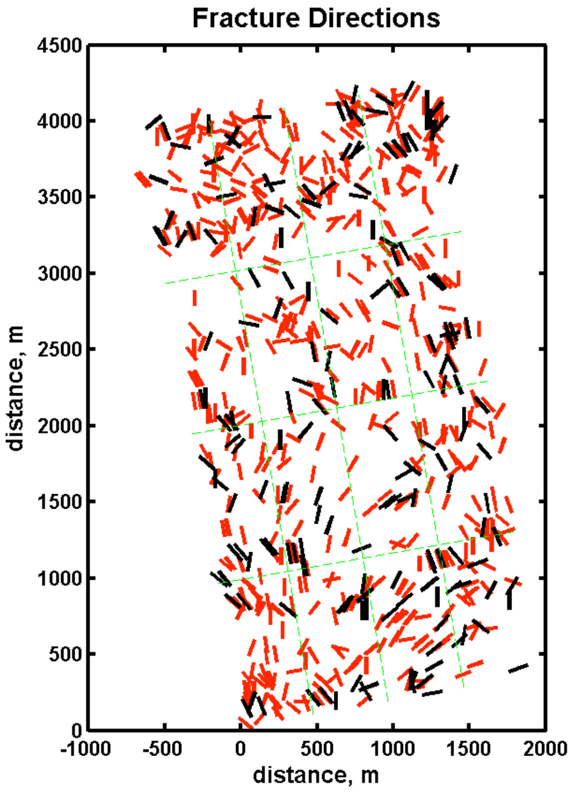

Figure 8. The spatial orientation and distribution of fractures over the field as indicated from scattering indices of multiple azimuthal stacks. The black and gray bars show the orientations for the top two bins of highest scattering indices. The dashed-line grid shows the location of the histogram plots in Figure 9.

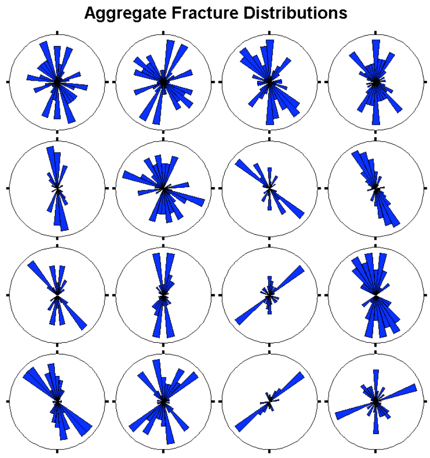

Figure 9. Angular histogram plots of the fracture distributions shown in Figure 8. Each plot represents the corresponding subportion of the field delineated by the dashed lines in Figure 8. The top of each plot represents fractures aligned North.

AVOA analysis was completed on the same data set. We use a surface-fitting algorithm for the AVOA analysis that is similar to the approach of Hall and Kendall (2003). Many azimuthal AVO studies separate the data into a few discrete azimuths and compare the individual AVO results in those directions. However, by analyzing the full range of azimuths simultaneously the problem is better constrained. An iterative, non-linear least squares inversion that uses the Gauss-Newton method is employed (Minsley et al., 2004). Figure 10 shows the results of this analysis at four well locations in the field and compares the fracture orientation to that obtained by Gaiser et al (2002) from shear wave birefringence.

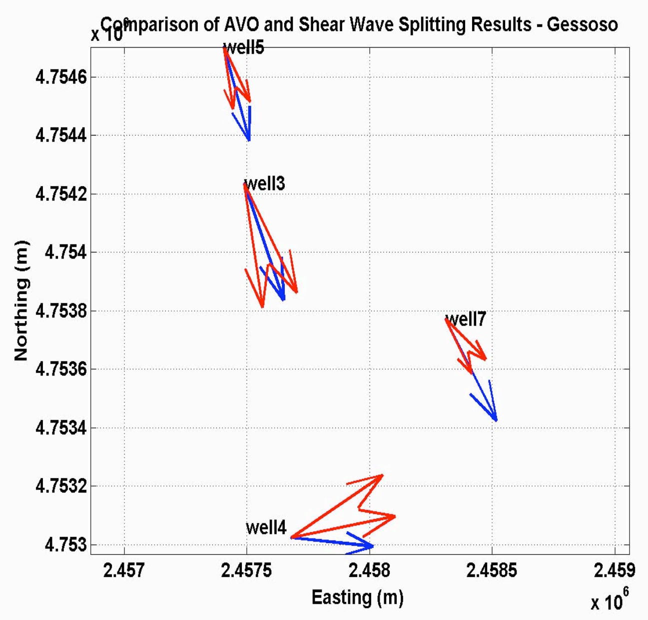

Figure 10. Comparison of the AVOA isotropy axis direction (blue) found in this study with fast S-wave direction (red) reported by Gaiser *et.al.* for the Gessoso horizon at four locations. Magnitude of the arrows represents the amount of anisotropy for each method at each location. Two fast S-wave arrows are used to show the 20° uncertainty of the direction.

CONCLUSIONS

Large-scale zones of fracturing control fluid flow in certain reservoirs, and such zones can scatter seismic energy depending on the fracture density and compliance, as well as the spacing relative to the seismic source wavelength. This scattered wave energy contains information about the fracture properties. Using numerical modeling data we developed two methods of analyzing scattered wave energy from fractured reservoirs. One method, a deconvolutional process that measures the 'ringiness' of the transfer function, can be used to estimate fracture orientation from azimuthally stacked data. This method was applied to field data from a fractured reservoir resulting in fracture orientation estimates that agree with published borehole and PS anisotropy studies, as well as AVOA analysis.

ACKNOWLEDGEMENTS

Our thanks to Lawrence Berkley Lab for use of their 3D finite difference modeling code. We would like to recognize and thank ENI S.p.A. AGIP, the Department of Energy Grant number DE-FC26-02NT15346, and the Earth Resources Laboratory Founding Member Consortium for funding and supporting this work. We greatly appreciate the support and suggestions offered by Laura Vetri of Agip.

REFERENCES

Angerer, E., Horne, S., Gaiser, J., Walters, R., Bagala, S., 2002, Characterization of dipping fractures using PS mode converted data, *7 2nd SEG Expanded Abstracts*.

Ata, E., and Michelena, R. J., 1995, Mapping distribution of fractures in a reservoir with P-S converted waves, *The Leading Edge*, **12**, 664-676.

Coates, R.T. and Shoenberg, M., 1995, Finite difference modeling of faults and fractures, *Geophysics*, **60**, 1514-1526.

Gaiser, J., Loinger, E., Lynn, H, and Vetri, L, 2002, Birefringence analysis at the Emilio field for fracture characterization, *First Break*, **20**, 505-514.

Hall, S.A. and Kendall, J.M. (2003). Fracture characterization at Valhall: Application of P-wave amplitude variation with offset and azimuth (AVOA) analysis to a 3D ocean-bottom data set. *Geophysics*, **68(4),** 1150-1160.

Lynn, H., Simon, K. M., and Bates, C. R., 1996, Correlation between P-wave AVOA and S-wave traveltime anisotropy in a naturally fractured gas reservoir, *The Leading Edge*, **15**, 931-935

Minsley, B., Willis, M., Krasovec, M., Burns, D., and Toksoz, M.N., 2004, Frcture detection using amplitude versus offset and azimuth analysis of a 3D P-wave seismic dataset and synthetic examples, *74th SEG Expanded Abstract.*

Nihei, K.T., et al., 2002, Finite difference modeling of seismic wave interactions with discrete, finite length fractures, *72nd SEG Expanded Abstracts*.

Vetri, L., Loinger, E. Gaiser, J. Grandi, A., Lynn, H, 2003, 3D/4C Emilio: Azimuth processing and anisotropy analysis in a fractured carbonate reservoir, *The Leading Edge*, 675-679.

Vlastos, S., Liu, E., Main, I.G., Li, X.Y., Numerical simulation of wave propagation in media with discrete distributions of fractures: effects of fracture sizes and spatial distributions, *Geophys. J. Int.*, **152**, 649-668.

In-Situ Stress Field from Breakouts and Flexural Wave Crossovers and Comparison with Plate Tectonic Models

Samantha Grandi K.

Abstract

In this paper we obtain in-situ stress information based on two methods. The first estimates stress directions from the orientation of breakouts in a borehole. Stress magnitudes are interpreted from elastic models of stress distribution around the borehole. The second method is applied where the borehole is not deformed and a crossover in the dispersions of polarized flexural waves is observed. Data rotation to principal axes provides stress orientation. Magnitudes are inferred from the velocity anisotropy measured at low frequencies.

For a particular field dataset we observe that the greatest stress is horizontal in the NNW-SSE direction ($SHmax$). Both methods agree in the estimation of stress orientation and magnitude. The relative magnitudes of principal stresses are on average $SHmax \simeq 1.1Sv$ (Sv: vertical stress) and $Shmin \simeq 0.9Sv$ ($Shmin$: minimum horizontal stress), suggesting predominantly strike slip tectonics. The estimated stress orientation is in agreement with a regional stress field calculated from the relative motion of the Caribbean and South America plates.

1 Introduction

In this paper stress information around a borehole is obtained independently from caliper data and cross-dipole well logs. First, the field data are presented and rock parameters, needed for the stress calculations, are derived. Following this, the methodology applied to infer stress orientation and magnitudes where the borehole is deformed is described. Principal stress directions are interpreted from the azimuths of the elongated sides of the borehole. To obtain the magnitudes, a range of values of horizontal stresses is modeled until the distribution around the borehole is such that the actual deformations are explained. It is assumed that rock failures occur when the stress exceeds the compressive rock strength. We use a second method to determine stresses in the intervals where the borehole is not deformed. This method is based on the observations of stress-induced anisotropy in cross-dipole data. Rotating the data to principal axes provides an estimation of the stress field orientation. Differences in the velocities of polarized flexural waves are measured, and comparing them to laboratory experiments where rock samples are compressed, approximated stress magnitudes are estimated.

There are well established methods to derive in-situ stress field; among them, breakout analysis, extended leakoff tests, earthquake focal plane mechanisms, and polarization of tube waves in VSP's (Zoback et al., 1986). Different evidences of stress can be found in well data. Breakouts, for instance, are unidirectional wellbore deformations due to large anisotropic far field stresses released around the cavity. Caliper dipmeter and image logs are records of this deformed state and therefore contain some stress information (Plumb and Hickman, 1985). In other cases, where the rock is strong enough not to break under the giving stress state, cross-dipole data record different elastic velocities depending on azimuth and radial distance, which in turn contain information of the stress field anisotropy (Sinha and Kostek, 1996). An integrated analysis of dipmeter and sonic data complements the limitations of both methods: the first is limited if breakouts are combined with other kinds of borehole instability that shadow or noise the data (washouts, key sets) (Cox, 1983); the second method is particularly inconclusive if the formation is fast and strongly anisotropic.

Within the lithosphere, the principal stress planes appear to be oriented horizontally and vertically. $SHmax$ describes the maximum principal horizontal stress and $Shmin$ the minimum principal horizontal stress. The vertical principal stress, Sv, is described as the stress induced by the weight of the overlying rock. Typically in the Earth, the vertical stress is the largest of the principal stresses, however, there are some areas, particularly at plate boundaries, where tectonic processes take place and one or both horizontal stresses can exceed the vertical one (Zoback and Zoback, 1989) (Addis et al., 1993).

To estimate stress magnitudes, few methods have been proved successfully. In practice, simple but weak assumptions are frequently made; namely, horizontal stresses are considered equal and related to the vertical stress by a function of Poisson's ratio. Such a relationship assumes that no deformations take place in the horizontal plane. Hydrofracture experiments provide reliable stress magnitudes as well as orientations, but this technique, being expensive and formation damaging, must be limited to specific locations. Zoback et al. (1985) determined the magnitude of horizontal principal stresses from measurements of the breakout's shape. This method has the shortcoming of assuming elastic failure and requiring the availability of borehole image logs which are less likely to be included in logging programs than standard caliper logs. Stress magnitudes can also be estimated from acoustic data. Huang et al. (2000) implemented a multifrequency inversion of borehole flexural and Stoneley wave dispersions based on a perturbation theoretical framework (Sinha and Kostek, 1996), and applied it to a particular data set of slow formations.

2 Field Data

A whole suite of logs at an in-land borehole location in Northeast Venezuela is available for the present analysis. The four-arms dipmeter tool provides two perpendicular measurements of the borehole diameter. One pair of arms align with the long axis and the other with the short axis in the case of a borehole of non-circular cross section. The determination of the azimuth of the elongated side is possible since the dipmeter includes a "General Purpose Inclinometry Tool"[1] that measures the sonde orientation with respect to the magnetic north everywhere downhole.

Figure 1 shows two depth sections of the wellbore where conditions are different. Apart from some rugosities and minor washouts, the borehole between 6500 and 8500 ft can be considered stable with no failures or "in gauge", its diameter being close to the bit size (12.25 in). This is the type of section where the second method introduced above will be implemented. In contrast, on the right of the same figure, two perpendicular diameters are shown between 9000 and 12000 ft. The borehole presents washout areas and enlargements, or cavings, reaching in some cases double the bit size. In some depths, one diameter is significantly larger than the other, indicating that the borehole shape has a certain ellipticity. We shall apply the first method to estimate stresses in borehole sections with these characteristics.

The dipmeter tool rotates as it moves uphole, which is evident from the tool orientation on the right of both intervals in figure 1. In the stable case, the tool completes about four full rotations in 2000 ft, whereas in the second section it barely rotates more than once over the same distance. The depth of the cavings into the formation interrupts the normal tool rotation.

In the following calculations, several formation properties are required. For instance, the model of in-situ stresses requires various inputs: elastic constants, pore pressure, fluid pressure in the borehole, and rock compressive strength at every depth. The dynamic elastic constants are derived from the P-wave velocity (V_p) and shear wave velocity (V_s) using equations:

$$\begin{aligned} E &= \rho V_s^2 \frac{3V_p^2 - 4V_s^2}{V_p^2 - V_s^2} \qquad (1) \\ \nu &= \frac{V_p^2 - 2V_s^2}{2(V_p^2 - V_s^2)} \end{aligned}$$

---

[1] Schlumberger's acronym GPIT

where E and ν refer to Young's modulus and Poisson's ratio respectively and ρ is the rock bulk density.

Rocks in-situ deform nearly statically; therefore, static rather than dynamic moduli are needed in a realistic model. Several empirical relationships, in order to obtain static parameters from dynamic measurements, have been reported. The static Young's modulus is calculated in this study using the procedure in Fjaer (1999) developed for weak sandstones. On average, the static-dynamic ratio is about 0.65 for these data.

The compressive strength (C_0) can be computed from well logs using the Coates and Denoo (1981) empirical relationship for consolidated rocks:

$$C_0 = 50000 E_s K_s (0.008 V_{sh} + 0.0045(1 - V_{sh})) \frac{cos\theta}{1 - sin\theta} \tag{2}$$

where E_s and K_s are the static Young's and bulk modulus, given in 10^6 psi, and θ refers to the angle of internal friction which is a function of rock consolidation (40° is suggested for sandstones). V_{sh} is the shale volume that can be computed from the gamma ray log. In general, log-derived compressive strength would require further calibration with core data. Static Young's modulus, Poisson's ratio, and rock compressive strength are shown in figure 2.

The variation of pore pressure with depth is assumed equal to the hydrostatic gradient (10 MPa/km), and the vertical stress is estimated from the integrated weight of the overburden:

$$S_v = \int \rho(z) g \, dz \tag{3}$$

Pore pressure, drilling mud pressure, and vertical stress are shown in figure 3. Calculated properties at a few specific depths are extracted in table 1.

As input to the second method, cross-dipole data are necessary. Cross-dipole acoustic information in this well is measured with the DSI[2] tool. This type of acquisition consists in alternating the firing of the upper and lower dipole sources, which are oriented orthogonally, and also alternating the receiving in the inline and crossline receivers (figure 4). In this way, four sets of 8 traces each are generated: 1. upper dipole source-inline receivers, 2. lower dipole source-inline receivers, 3. upper dipole source-crossline receivers, and 4. lower dipole source-crossline receivers. The two middle sets are called the cross-components. The crossline receivers are the hydrophone pairs oriented parallel with the upper dipole source, whereas the inline receivers are oriented parallel with the lower dipole source. The sampling interval is 40 μsec, and the sources operate at low frequencies (with peak frequency around 2 kHz). The phase difference introduced by the

---

[2] Dipole Shear Sonic Imager. Mark of Schlumberger.

Table 1: Formation parameters at various depths. Static Young's modulus (E_s) is in GPa; pore (P_p) and mud pressure ($Pmud$), vertical stress (S_v), and strength (C_0) units are MPa. R_{max} refers to the maximum borehole radius in meters.

Depth[ft]	E_s	ν	C_0	Pp	Pmud	S_v	R_{max}
5610	24.33	0.32	40.85	17.11	16.84	39.8	0.18073
5815	33.03	0.2296	45.91	17.74	17.45	36.03	0.1594
6700	38.21	0.2107	75.45	20.44	20	42.89	0.1619
7100	44.59	0.1839	78.28	21.66	21.68	45.97	0.1652
7510	32.64	0.248	61.5	22.91	22.81	54.2	0.1715
8680	32.24	0.2781	66.26	26.47	26.02	58.19	0.1593
8760	39.57	0.233	52.44	26.72	26.26	58.81	0.18013
9330	42.95	0.128	65	28.46	28.43	68.13	0.18784
10120	29.55	0.31	57.03	30.87	31.02	69.4	0.20399
10980	31.69	0.266	55.05	33.49	33.42	80.75	0.25899
11700	43.12	0.182	61.98	35.69	35.58	81.75	0.23847
12130	38.23	0.29	86.28	36.89	36.99	89.64	0.20259
12750	33.98	0.2524	55.05	38.89	4099	89.88	0.1604

separation of the sources and the delay between firings is corrected for in the field (B. Sinha - Schlumberger-Doll Research, personal communication). The main borehole wave recorded at such frequencies and with this source symmetry (dipole) is the flexural mode. This wave is dispersive at logging frequencies.

3 Method I: Borehole Deformations

In order to infer the stress field, the first method uses the observations of the borehole cross-sectional area at every depth level. This information is obtained from standard caliper tools, four or three arms dipmeter tools, or image logs.[3]

The borehole can present instabilities as a consequence of one or several processes acting together, such as chemical reactions between mud components and some formation minerals, time-dependent changes in pore pressure, well deviation, high angle of penetration relative to bedding dip, reinitiated fractures, and so forth. In particular, the wellbore can deform as a response to stress. These special deformations are referred to as "breakouts" in the oil industry. Breakouts are localized compressive shear failures.

Breakouts occur symmetrically (180 deg. apart) and at a consistent azimuth throughout the well section that corresponds to the minimum horizontal stress and the maximum concentration of compressive stress near the borehole. Since the borehole diameters and their orientation can be measured at every depth, these

---

[3] Image logs provide a 360° ultrasonic or resistivity image of the borehole wall.

data provide a means of estimating principal stress directions.

The occurrence of stress-induced failures around a borehole is explained in terms of the hoop stress accumulation relative to the strength of the rock surrounding the well. Stresses around a circular hole in a homogeneous, isotropic, elastic plate subjected to maximum and minimum effective stresses in the far field and a fluid pressure in the hole are given by Jaeger and Cook (1979):

$$\begin{aligned}
\sigma_r &= \frac{1}{2}(SHmax + Shmin)(1 - \frac{R^2}{r^2}) + \frac{1}{2}(SHmax - Shmin)(1 - 4\frac{R^2}{r^2} + 3\frac{R^4}{r^4})\cos(2\theta) + \frac{\Delta P R^2}{r^2} \\
\sigma_\theta &= \frac{1}{2}(SHmax + Shmin)(1 + \frac{R^2}{r^2}) - \frac{1}{2}(SHmax - Shmin)(1 + 3\frac{R^4}{r^4})\cos(2\theta) - \frac{\Delta P R^2}{r^2} \qquad (4) \\
\tau_{r\theta} &= -\frac{1}{2}(SHmax + Shmin)(1 + 2\frac{R^2}{r^2} - 3\frac{R^4}{r^4})\sin(2\theta)
\end{aligned}$$

where σ_r is the radial stress, σ_θ is the circumferential stress, $\tau_{r\theta}$ is the tangential shear stress, R is the radius of the hole, θ is the azimuth measured from the direction of $SHmax$, and ΔP is the difference between the fluid pressure in the borehole and that in the formation (positive indicates excess pressure in the borehole); $SHmax$ and $Shmin$ refer to the effective horizontal stresses, that is, the stresses supported by rock and pore fluid.

Hoop stress is defined by equation 4 when $r = R$. Figure 5 shows the variation of hoop stress as a function of azimuth for different values of $SHmax$ and $Shmin$. Hoop stresses are maximum at 90° and minimum at 0°:

$$\begin{aligned}
\sigma_{0^\circ} &= 3Shmin - SHmax - \Delta P \\
\sigma_{90^\circ} &= 3SHmax - Shmin - \Delta P \qquad (5)
\end{aligned}$$

Failure occurs when the strength of the rock is exceeded by the concentrated stress. For instance, if the rock had a strength $C_0 = 150\ MPa$, as shown in figure 5, failure around the borehole would be restricted to the angle ranges $\theta = -45^\circ$ to -90° and 45° to 90°, given $SHmax = 2.2\ Sv$ and $Shmin = 1.25\ Sv$. Not to have any failures under this stress field, the rock has to have a compressive strength larger than 250 MPa. On the contrary, if it is as weak as 25 MPa, it will fail at all azimuths. The function σ_θ steepens as the difference between $SHmax$ and $Shmin$ becomes large.

3.1 In-Situ Stress Elastic Model

Figure 5 suggests that borehole failures also contain information about the relative magnitude of the stresses. Based on an elastic approach, we solve for the concentration of stresses around the borehole and compare hoop stress values with rock strength.

Unless the rock column is being deformed by compaction, the deformations of a borehole are confined to the horizontal plane, perpendicular to the borehole axis. Such a case is represented in elasticity under the plane strain assumption where no deformations take place in the z-direction (borehole axis), and the displacements in x and y are only functions of x and y but not z: $\epsilon_z = \gamma_{yz} = \gamma_{zx} = 0$, where ϵ_z is the normal strain in the z-direction and γ_{yz} and γ_{zx} are shear strains.

An infinitely thin plate containing a circular hole and under plane strain represents a borehole subjected to far field stresses. In the model, the particle displacements in x and y (u and v) are computed at every point solving Navier's equations in static equilibrium:

$$\begin{aligned} -\frac{\partial}{\partial x}[c_1\frac{\partial u}{\partial x} + c_2\frac{\partial v}{\partial y}] - \frac{\partial}{\partial y}[c_3(\frac{\partial u}{\partial y} + \frac{\partial v}{\partial x})] &= 0 \\ -\frac{\partial}{\partial x}[c_3(\frac{\partial u}{\partial y} + \frac{\partial v}{\partial x})] - \frac{\partial}{\partial y}[c_2\frac{\partial u}{\partial x} + c_1\frac{\partial v}{\partial y}] &= 0 \\ -\frac{\partial}{\partial y}[c_3(\frac{\partial u}{\partial y} + \frac{\partial v}{\partial x})] - \frac{\partial}{\partial z}[c_2(\frac{\partial u}{\partial x} + \frac{\partial v}{\partial y})] &= 0 \end{aligned} \tag{6}$$

where body forces are disregarded, and $c1$, $c2$, and $c3$ are the only non-zero components of the isotropic material constants tensor. In terms of Young's modulus and Poisson's ratio:

$$\begin{aligned} c_1 &= \frac{E(1-\nu)}{(1+\nu)(1-2\nu)} \\ c_2 &= \frac{\nu E}{(1+\nu)(1-2\nu)} \\ c_3 &= \frac{E}{2(1+\nu)} \end{aligned} \tag{7}$$

Once the displacements are solved, the normal and shear strains in the x-y plane are obtained by taking derivatives. To get stresses, strains and the stiffness matrix are substituted into the linear elastic constitutive relation. Normal stresses in the z-direction are not neglected; however, by Hooke's law shear stresses in the z-plane vanish.

A numerical solution of equations 6 at every point is found using a finite element approximation.[4] The

---

[4] We use the commercial program Femlab by Comsol.

radius of the undeformed borehole is chosen as in the case data, 0.1555 m. The area is meshed with curved triangular elements that refine towards the borewalls. In order to obtain a stable solution, boundary conditions must be imposed. The outer edges are considered fixed in the direction perpendicular to the stress applied. At the same borders, forces per unit area representing the far field stresses are specified, $SHmax = F_x$ and $Shmin = F_y$. Force per unit area corresponding to the mud pressure is specified at the boundary of the hole (fig. 6).

Stresses in porous media are dependent on fluid pressures in cracks and pores. To take into account the presence of fluid, effective stresses are the actual magnitudes sought. Effective stresses are related to total stresses through Terzaghi's law (Bourbie et al., 1987); for example, the maximum horizontal effective stress is defined as:

$$SHmax = SH - \alpha P_p \tag{8}$$

where SH represents the total stress, P_p is the pore pressure, and α is the Biot constant taken as 1 hereinafter.

The modeling is performed at each depth level and iterated for different boundary conditions (i.e. the far field stresses) until the hoop stress equals the rock strength at a radial distance that coincides with the long radius of the borehole. Borehole size is known from the 4-arms caliper measurement. Because there is a breakout at the modeled depth, stresses are assumed to have exceeded the rock mechanical resistance, leading to failure and resulting in an elongated borehole cross section. Hoop stresses are expected to be different around the hole and maximum compressive in the direction of the smallest stress acting in the far field.

Calculated stresses at every point in the region are related to cylindrical stresses by the linear system (Huang et al., 2000):

$$\begin{bmatrix} \sigma_x \\ \sigma_y \\ \sigma_{xy} \end{bmatrix} = \frac{1}{x^2 + y^2} \begin{bmatrix} x^2 & y^2 & -2xy \\ y^2 & x^2 & 2xy \\ xy & -xy & x^2 - y^2 \end{bmatrix} \begin{bmatrix} \sigma_r \\ \sigma_\theta \\ \tau_{r\theta} \end{bmatrix} \tag{9}$$

A solution for displacements is obtained in cartesian coordinates and the analysis of the hoop stress distribution requires a coordinate transformation of the stress field. Hoop, radial, and tangential stresses are obtained solving system 9. The normal stress in the axial direction is obtained by:

$$\sigma_z = \nu(\sigma_r + \sigma_\theta) \tag{10}$$

3.2 Results

3.2.1 Stress Directions

The field data are classified according to the borehole radius into sections where the borehole is considered stable and intervals where it presents some instabilities (i.e. one diameter is significantly larger than the bit size). In the latter case, the orientation of the elongated size of the borehole is calculated from the GPIT data. After correcting by the magnetic declination and summing the contributions from orientations separated by 180°, a histogram of azimuths is plotted in figure 7. The dominant azimuths are observed between 250° and 260°. Since they are consistent on the well section, the corresponding elongated borehole cross-sections are considered breakouts.

At 10120 ft, for instance, the borehole has a breakout. The long diameter is 16 in whereas the minor axis length is about 13.5 in (bit size: 12.25 in). The larger axis is at 253° with respect to the geographic north. Since breakouts align with the minimum horizontal stress, $Shmin$ is also oriented at 253° azimuth. Thus, $Shmin$ strike is about ENE-WSW and $SHmax$ is oriented NNW-SSE (figure 8).

3.2.2 Stress Magnitudes

Following the procedure described, we solve for hoop stresses in the region around the borehole for a range of combinations of maximum and minimum horizontal stresses. The actual magnitudes of $SHmax$ and $Shmin$ acting on the far field are those that induce the accumulation of hoop stresses greater than rock strength up to the deformed borehole radius. The maximum horizontal stress magnitudes are varied between 0.8 S_v and 1.5 S_v. $Shmin$ is increased from 0.6 S_v to 1.45 S_v.

For instance, boundary conditions of $Shmin = 69.39\ MPa$ and $SHmax = 76.33\ MPa$ are specified on the horizontal and vertical outer edges of a model that represents the formation at 10120 ft (parameters are specified in table 1). Calculated hoop stresses are shown in figure 9. As expected, the maximum concentration of stresses occurs at the azimuth of $Shmin$ (north-south in the figure), the region that undergoes compressive failure. Caliper data indicates that a breakout at this depth increments the borehole radius in the direction of $Shmin$ to about 0.204 m; that is, about 5 cm larger than the nominal size. The short axis is approximately its non-deformed length.

Resultant hoop stresses for such far field values are larger than the compressive strength of the rock from the non-deformed borehole wall to a depth of about 5 cm into the formation. Hoop stresses at the azimuth of $SHmax$ are not enough to overcome the strength of the rock, hence no failure is predicted at this location.

Given that this hoop stress distribution explains the observations at 10120 ft, the far field stresses applied as boundary conditions are interpreted as the in-situ horizontal stresses.

The vertical stress needs to be recomputed in order to take into account the normal stress (equation 10). The new S_v comes from the vertical stress calculated from the overburden plus σ_z. In terms of the vertical stress, the relative magnitudes found at 10120 ft are $SHmax \simeq 0.9893\ S_v$ and $Shmin \simeq 0.9134\ S_v$.

The iterated modeling and analysis is performed every 10 ft in the breakout sections of the well. Depths where a combination of washouts and breakouts is suspected are not modeled. Similarly, depths where the elongated size seems to be larger than the maximum extension of the caliper tool are left out. Relative horizontal to vertical stresses magnitudes are obtained and shown in figure 10. The maximum horizontal stress varies between 0.91 and 1.1612 times the vertical stress, and the minimum horizontal stress remains the smallest in the whole depth section, with values ranging between 0.7781 and 1.0361 S_v. These relative magnitudes indicate that the area is under a combination of strike slip tectonics, in which the vertical is the intermediate stress, and normal faulting, in which the vertical stress is the largest. Colmenares and Zoback (2003) characterise northeastern South America with the same combination of stress regimes.

4 Method II: Stress-induced Velocity Anisotropy

The second method to obtain stress information is based on crossovers observed in the dispersion of flexural waves as recorded in cross-dipole logs. The flexural wave corresponds to the normal mode whose azimuthal order is 1, meaning that pressures in the fluid and displacements in the solid change sign at 180° (Ellefsen, 1990). For typical logging frequencies only the lower order radial modes are excited. The flexural wave velocity approaches the formation shear wave velocity at low frequencies and the compressional fluid velocity at the high frequency end (figure 11). This wave does not possess a theoretical cutoff, but its excitation becomes extremely small below a transition frequency leading to an effective cutoff; in practice this is at about 2 kHz.

Acoustic velocities in sedimentary rocks depend on the state of stress. They increase with increasing external hydrostatic stress, and the increment gradually becomes smaller. Similarly, velocities increase with effective pressures (Bourbie et al., 1987). Such behaviour is attributed to the increase of the rigidity or stiffness of the rock matrix when a hydrostatic compressive stress is applied. The variations in velocity under a uniaxial stress depend on the direction of wave propagation with respect to the direction of applied stress. Cracks, or any soft inclusion in the material that is preferentially aligned perpendicular to the direction of the applied stress, close under low effective pressures and an uniaxial stress, while cracks oriented parallel would open. As a consequence, the rock becomes stiffer in the direction of the applied stress and waves propagating in this direction travel faster, thus creating an anisotropic velocity field (Fjaer and Holt, 1994). Shear waves polarize into a slow and a fast direction in the presence of an uniaxial compressive stress with the fast shear wave polarization being parallel to the applied stress direction, or equivalently, normal to the preferential orientation of fractures, pores, or grains (figure 12). In the case of an homogeneous and intrinsically isotropic formation, the elastic velocity anisotropy is attributed to the stress field (Winkler, 1997).

In the presence of a borehole, as explained above, the stress distribution must adapt to the circular boundary condition by deforming around it. The circumferential stress increases and the maximum compressive stress concentrates in the direction where the far field stress is less compressive. Therefore, the rock stiffness changes radially as well as azimuthally, and elastic waves observe it. In particular, flexural waves, which travel parallel to the borehole axis, split in the horizontal plane, and because these waves are dispersive, they are sensitive to the radial change in properties (Winkler et al., 1998). At low frequencies, flexural waves have long radial depth of investigation and are not significantly affected by the stress-induced altered zone. As frequency increases, flexural waves (and all surface modes) become localized at the borehole wall; thus they are influenced by the near field stresses around the borehole. As a result, the dispersion curves of flexural waves recorded by two perpendicular dipoles are expected to cross at some frequency (figure 13).

An appropriate rotation of the cross dipole waveforms to the principal flexural wave polarization maximizes the crossover and provides the angles to the fast and slow direction. Knowing the orientation of the dipole, the direction of the maximum horizontal stress is deduced. On the other hand, the difference in velocities at the far field (low frequencies) in the two orthogonal directions can be compared to experimental results in which shear velocity is measured as confining pressure is increased. In such a way, assuming the vertical stress is the intermediate stress, the ratio of the principal stresses is determined. Since the vertical stress is estimated from the overburden, values of horizontal stress can be calculated.

Analysis of flexural wave crossover needs to be done in locations where the borehole is stressed but not deformed. Crossovers are indicators of stress induced anisotropy dominating over other sources of anisotropy.

4.1 Results

4.1.1 Stress Directions

Due to the tool rotation in its way uphole, cross-dipole data need to be rotated at each depth in order to align the dipole's orientation with the principal axes of anisotropy. Figure 14 shows some example depths where crossovers are observed. At these depths, the stress concentration has not exceeded the strength of the rock. As a consequence, the borehole is stable in the sense that its original radius is preserved. Since stress has not been released, waves in the surrounding rock propagate with different velocities depending on the polarization direction with respect to the orientation of minimum and maximum horizontal stresses. At these levels we are unable to apply the first method to estimate stresses since no failure is taking place; however, the crossover on the dispersion of flexural waves contains information about the principal stress directions, as explained before.

For instance, at 6700 ft the crossline component is oriented in such a way that the low frequency flexural wave arrives earlier (or travels faster) than the flexural wave polarized in the orientation of the upper dipole source (top left plot in figure 14). The upper dipole source is oriented at 55° azimuth; hence, the lower dipole is at 145°. Before rotating the data we already know that the maximum stress direction should not be oriented more than 90° apart from the actual position of the tool, otherwise the upper dipole would have registered the fast component at low frequencies, and this is not the case. Therefore, the fast direction must be limited to the range between 55° and 235° azimuth.

The dispersion curves in figure 15 are obtained after rotating the data using a method that minimizes the energy on the waveforms recorded by the cross-components.[5] Such a rotation method neglects the dispersive character of the flexural wave and is very sensitive to the time window length chosen to compute the angles (Nolte et al., 1997). For the data at 6700 ft, the angle of the fast orientation is about 32°. Adding this value to the tool orientation indicates that the direction of the maximum far field stress is 177° (or 357°) azimuth.

The same analysis was performed at several other depths. The maximum stress orientations obtained with this technique vary in the range between 334 and 14 degrees azimuth. Figure 16 shows minimum horizontal stress azimuth at some depths derived from both methods. Mean values agree to within 10 degrees. We conclude that maximum horizontal stress runs approximately NNW-SSE, hence $Shmin$ lies in the east-west direction.

To investigate if the direction of the principal stresses derived from the in-situ measurements correspond to the regional tectonic stress field, an intraplate stress distribution is calculated in the appendix. Only tractions at plate boundaries are considered; therefore, the model is purely kinematic and largely simplified by assuming constant velocities along main boundary segments. The results (displayed in figures 23 and 24) agree with the orientation of the in-situ stresses here obtained.

---

[5] Code by Dr. Beltram Nolte and Dr. Xiaojun Huang while at MIT, ERL.

4.1.2 Stress Magnitudes

The situation of one stress orientation being dominant in the Earth can be compared to laboratory experiments where rock samples are submitted to different confining pressures. For instance, Lo et al. (1986) measured ultrasonic P, SH, and SV wave velocities in sample rocks of a typical granite, shale, and sandstone, while varying the confining pressure from 5 to 100 MPa. The experiments were performed for several directions of wave propagation. For Berea sandstone, velocities were measured parallel, perpendicular, and at an oblique direction with respect to bedding. Samples were not saturated. The results suggest that Berea sandstone is transversely isotropic and therefore satisfies the condition of isotropicity required by the stress-induced anisotropy method. Figure 17 shows two orthogonal shear wave velocities reported in Lo et al. (1986) corresponding to a perpendicular direction of propagation with respect to bedding planes. We based our next calculations on the experimental results presented in figure 17.

The estimation of stress magnitudes from the cross-dipole data begins by measuring flexural wave velocity anisotropy at low frequencies; that is, previous to the crossover occurrence and where energy content peaks. Together with mud pressure, anisotropy percentages and differences between fast and slow velocity observed at some depths are listed in table 2. We proceed by calculating the velocity corresponding to where confining and mud pressure are equal according to the experiments on Berea sandstone. Such pair velocity-stress represents the intermediate stress conditions, or in this case, the vertical stress close to the borehole. The difference in velocity measured from the orthogonal flexural waves is centered at these coordinates in the

Table 2: Velocity anisotropy at the far field and mud pressure (MPa) at some crossover depths

Depth[ft]	Anisotropy %	ΔV_s m/s	Pmud
5815	2.78	56	17.45
6115	1.86	44	18.56
6490	2.44	44	19.72
6700	0.897	22	20
6772.5	2.89	80	20.39
7000	5.12	99	21.37
7100	3.41	89	21.68
7445	10.44	255	22.62
7500	4.43	99	22.78
8000	1.5	36	24.35
8120	4.78	117	24.82
8280	2.51	66	25.18
8680	2.45	47	26.02
12750	2.46	49	40.99

velocity-stress plane for the Berea sandstone, and the corresponding limiting stresses are estimated. Finally, ratios between maximum and minimum stress with respect to confining pressure are calculated. We assume these ratios to be similar to the relative magnitudes of principal in-situ stresses.

To exemplify the procedure, let us take the case depth at 6700 ft. Mud pressure is 20 MPa and Berea sandstone shows a shear velocity of 2480 m/s at this confining pressure. The anisotropy measured on the rotated cross-dipole data, as shown in figure 15, is 22 m/s (at around 2 kHz, the peak frequency). This difference between fast and slow velocities translates into the velocity range 2469 to 2491 m/s for the experimental results. Confining pressures of 19.09 and 21.4 MPa are predicted for these velocities and by taking their ratio with the mud pressure, we obtain $Shmax/Sv = 1.07$ and $Shmin/Sv = 0.9545$. Figure 18 shows the results at this and other depths. $SHmax/Sv$ ratios vary between 1.07 and 1.2962. $Shmin/Sv$ ranges between 0.7788 and 0.9545. Mean values estimated are $SHmax/Sv = 1.1663$ and $Shmin/Sv = 0.8602$. With an estimation of overburden, absolute values of horizontal stress can be calculated. The combined results of methods 1 and 2 are shown in figure 19.

5 Conclusions

The orientation of horizontal principal stresses has been obtained by a combination of breakout analysis, and flexural wave crossovers, and from regional stress models calculated from plate motions. Borehole methods give the maximum horizontal stress direction to be slightly west of north. Specifically, breakouts indicate that $SHmax$ is oriented at 345±5° azimuth (measured clockwise from North), whereas the range derived from crossdipole data rotation is wider, between 334 and 14°. One of the main advantages of doing this kind of integrated data analysis is that flexural waves can provide stress information in those places where breakouts do not occur. Maximum stress direction from regional stress models ranges from 314° to 2.5° azimuth depending on plate motion constraints. In conclusion, all methods suggest that $SHmax$ is oriented NNW-SSE.

The magnitudes of horizontal stresses obtained by modeling stress distributions around the borehole and matching the static deformed state suggest that the intermediate stress is the vertical. Stress ratios determined by comparing velocity anisotropy with stress differences in experiments on Berea sandstone confirm that horizontal maximum stress and minimum stress magnitudes are about 1.1 and 0.9 times the vertical stress, respectively.

6 Acknowledgements

We thank the former Exploration Division of PDVSA for providing the field data. This work was supported by DOE Grant No. $DE-FC26\_02NT15346$ and the Borehole Acoustics and Logging Consortium of the Earth Resources Laboratory at MIT. The authors thank especially Dr. Xiaojun Huang, Dr. Rama Rao, Franklin J. Ruíz, and Dr. Randolph Martin for valuable discussions.

A Appendix: Regional Stress Model

In order to determine the regional stress directions, a finite element solution is computed for a model representing the relative motion between the Caribbean and South American plates. The process is similar to the one described in section 3.1 except that a plane stress approximation of the elasticity equations is assumed.

Plates' geometry is obtained from digital maps[6] corresponding to the model NUVEL-1A (DeMets et al., 1994). Figure 20 shows the model features and the location of the well. In the same figure we have shown a map of the main tectonic plates in the area of study. As observed, the model geometry represents fairly the dimensions and location of the Caribbean and South American plates. Figure 21 depicts the finite element mesh which refines toward the boundary Caribbean-South America.

Displacement conditions are specified in all boundaries by solving ordinary differential equations of the form:

$$\frac{\partial \mathbf{u}}{\partial t} = \mathbf{U} \tag{11}$$

where $\mathbf{u}$ is the displacement vector. $\mathbf{U}$ represents East and North components of the velocity, assumed constant along the particular boundary. Plate velocity can be obtained from global models describing the motion of a certain number of assumed-rigid plates. These global models are in general based on the geomagnetic reversal time scale, transform fault azimuths, earthquake slip vectors and more recently, on space geodetic measurements. In table 3 we have listed the East and North velocities corresponding to plate boundary locations with coordinates at about the center of the model edges, numbered as shown in figure 20. For comparison, Euler vectors from three different global models were used in the velocity calculations: NUVEL-1A (DeMets et al., 1994) (DeMets et al., 1990); REVEL (Sella, 2002); and the 2004 version of GSRM[7] (Kreemer et al., 2003). Edge 11, representing the limit between the South America and

---

[6] http://jules.unavco.org/GMT/

[7] Global Strain Rate Map, http://gsrm.unavco.org/intro/

North America plates is left fixed (zero displacement condition). Figure 22 shows the velocities from REVEL specified at the model boundaries.

At the well site the maximum compressive principal stress is oriented 33 degrees west of north if REVEL velocities are imposed (figure 23). NUVEL-1A velocities give an azimuth of 2.5 degrees for the $SHmax$ direction while GSRM velocities, being similar to REVEL, result in an orientation of 36 degrees west of north. The solution is not sensitive to conditions imposed on edges far from the well but it is highly sensitive to the relative velocity Caribbean-South America and Nazca-South America. The relative motion between the Caribbean and South America plate fits poorly with NUVEL-1A and other models (Weber et al., 2001). However, recent GPS measurements (Pérez et al., 2001) suggest that along the San Sebastián - El Pilar fault system, the Caribbean plate moves at a rate of 20.5 ± 2 mm/yr with an azimuth of N84±2°E. Such velocity is similar to the one assigned as the boundary condition according to the models REVEL and GSRM. In general, NUVEL-1A velocities at edges 5, 9 and 10 are about 50% slower than the other two more recent models, which incorporate present day rates in contrast to NUVEL-1A that averages motion over 3 million years. Increasing the Caribbean plate velocity relative to fixed South America has the effect of rotating the maximum stress to the west.

Nazca's velocity relative to stable South America is overestimated by approximately 15% in NUVEL-1A with respect to REVEL and GSRM. This difference has been interpreted as a deceleration in the convergence Nazca-South America, probably related to the Andes growth initiated about 20 Ma (Norabuena et al., 1999). Unlike the Caribbean-South America boundary zone, that is characterised by a predominantly strike-slip motion, Nazca plate subducts beneath South America. Moreover, it has been observed that site velocities decrease from the interior of Nazca plate to the interior of South America (Norabuena et al., 1998) indicating that only a percentage of the plate velocity measured at GPS stations on the Nazca plate should be associated with the continental deformation. Norabuena et al. (1998) estimate that about 50% of the overall convergence is accumulated on the locked plate interface, squeezing South America, and released in earthquakes. Another 20%, i.e. 12 to 15 mm/yr, is related to crustal shortening forming the Andes. The remaining 30% of the net convergence is associated to stable sliding of the Nazca plate.

A decrease in the velocity at the boundary Nazca-South America in our model also rotates the direction of principal maximum stress towards the west. For instance, a 50% decrease of REVEL velocities on edges 4 and 7 (Nazca-South America boundaries), rotates the orientation of maximum stress 12° counterclockwise with respect to the orientation found previously. Therefore, $SHmax$ azimuth falls within the range 315-327°. Similarly, reducing GSRM model velocities yields $SHmax$ azimuth between 314-324°. A corresponding

319° azimuth is obtained when half of the velocity predicted by NUVEL-1A is assigned to the Nazca-South America boundaries (figure 24).

In comparison with the principal stresses direction estimated from well-bore breakouts and acoustic data, the regional model provides consistent results, that is, $SHmax$ is oriented NNW-SSE (figure 24). Combining both borehole methods, $SHmax$ azimuth is observed at 345° and this is about 20° away from the most likely direction found with the global models.

Stress orientation calculated mostly from focal mechanisms is available at the World Stress Map (Reinecker et al., 2003). Data corresponding to events close to the well location are also indicated in figure 24 where it can be observed that the average $SHmax$ azimuth estimated with this method is about 330°.

Table 3: North and East plate velocities and boundary conditions used in the regional stress models. All velocities are in mm/yr. CA: Caribbean, CO: Cocos, NA: North America, NZ: Nazca, SA: South America, AN: Antarctic, ST: Scotia, AF: Africa

Edge #	Description	REVEL N	REVEL E	GSRM N	GSRM E	NUVEL-1A N	NUVEL-1A E
1	CA-CO	72.69	32.4	72.69	32.4	70.95	37.54
2	CA-NA	5.04	18.45	5.1	18.01	1.84	11.27
3	CA-NZ	12.52	28.67	10.26	29.07	14.09	47.05
4	NZ-SA (north)	14.06	66	12.82	63.74	16.76	76.93
5	CA-SA (west)	-2.27	21.63	-0.8	20.97	-1.87	14.15
6	SA-AN (west)	1.97	18.68	0.09	16.53	1.05	20.38
7	NZ-SA (south)	11.53	69.15	10.56	65.51	14.16	78.32
8	SA-ST	2.48	15.45	4.47	4.35	2.6	4.98
9	CA-SA (central)	0.71	20.04	1.84	19.56	0.3	13
10	CA-SA (east)	2.17	18.33	3.13	18.05	1.37	11.78
12	SA-AF (north)	-1.96	-25.43	-1.75	-26.03	-1.5	-28.35
13	SA-AN (southeast)	-2.35	-12.43	0.8	-12.38	-0.66	-15.88
14	SA-AF (northeast)	-4.23	-27.66	-3.73	-28.01	-4.06	-30.88
15	SA-AF (southeast)	-6.53	-29.83	-5.74	-29.32	-6.69	-33.52
16	SA-AF (southeast)	-7.52	-27.18	-6.62	-26.32	-7.85	-30.68
17	SA-AF (northeast)	-6.64	-29.83	-5.84	-29.75	-6.82	-33.41

References

Addis, T., Boulter, D., Roca-Ramisa, L., and Plumb, D. (1993). The Quest for Borehole Stability in the Cusiana Field, Colombia. *Oilfield Review.*

Bourbie, T., Coussy, O., and Zinszner, B. (1987). *Acoustics of Porous Media.* Editions Technip. Institute Français du Pètrole publications.

Brie, A., Codazzi, D., Denoo, S., Mueller, M., and Plona, T. (1998). New Directions in Sonic Logging. *Oilfield Review.*

Coates, G. R. and Denoo, S. (1981). Mechanical Properties Program using Borehole Analysis and Mohr's Circle. *SPWLA 22nd. Annual Logging Symposium*, pages DD 1– 16.

Colmenares, L. and Zoback, M. D. (2003). Stress field and seismotectonics of northern South America. *Geology*, 31:721–724.

Cox, J. W. (1983). Long-axis Orientation in Elongated Boreholes and its Correlation with Rock Stress Data. In *24th Annual Logging Symposium*, page J, Calgary. Soc. of Prof. Well Log. Anal.

DeMets, C., Gordon, R. G., Argus, D. F., and Stein, S. (1990). Current plate motions. *Geophysical Journal International*, 101:425–478.

DeMets, C., Gordon, R. G., Argus, D. F., and Stein, S. (1994). Effect of recent revisions to the geomagnetic reversal time scale on estimates of current plate motions. *Geophysical Research Letters*, 21(20):2191–2194.

Ellefsen, K. J. (1990). *Elastic Wave Propagation Along a Borehole in an Anisotropic Medium.* PhD thesis, Massachusetts Institute of Technology.

Fjaer, E. (1999). Static and Dynamic Moduli of Weak Sandstones. *Rock Mechanics for Industry*, pages 675–681.

Fjaer, E. and Holt, R. M. (1994). Rock Acoustics and Rock Mechanics: Their Link in Petroleum Engineering. *The Leading Edge*, pages 255–258.

Huang, X., Zhu, Z., Toksöz, M. N., and Burns, D. R. (2000). Effects of formation stress on logging measurements. pages 10.1–10.21. Borehole Acoustics Logging and Reservoir Delineation Consortia, Earth Resources Laboratory, MIT.

Jaeger, J. C. and Cook, N. G. (1979). *Fundamentals of Rock Mechanics.* Chapman and Hall, London.

Kreemer, C., Holt, W. E., and Haines, A. J. (2003). An integrated global model of present-day plate motions and plate boundary deformation. *Geophysical Journal International*, 154:8–34.

Lo, T., Coyner, K. B., and Toksöz, M. N. (1986). Experimental determination of elastic anisotropy of Berea sandstone, Chicopee shale and Chelmsford granite. *Geophysics*, 51(1):164–171.

Nolte, B., Rao, R., and Huang, X. (1997). Dispersion Analysis of Split Flexural Waves. pages 12.1–12.25. Borehole Acoustics and Logging and Reservoir Delineation Consortia, Earth Resources Laboratory, MIT.

Norabuena, E., Leffler-Griffin, L., Mao, A., Dixon, T., Stein, S., Sacks, I. S., Ocola, L., and Ellis, M. (1998). Space Geodetic Observations of Nazca-South America Convergence Across the Central Andes. *Science*, 279.

Norabuena, E. O., Dixon, T. H., Stein, S., and Harrison, C. G. A. (1999). Decelerating Nazca-South America and Nazca-Pacific Plate Motions. *Geophysical Research Letters*, 26:3405–3408.

Pérez, O., Bilham, R., Bendick, R., Velandia, J. R., Hernandez, N., Moncayo, C., Hoyer, M., and Kozuch, M. (2001). Velocity field across the southern Caribbean plate boundary and estimates of Caribbean/South-American plate motion using GPS geodesy 1994-2000. *Geophysical Research Letters*, 28(15):2987–2990.

Plumb, R. A. and Hickman, S. H. (1985). Stress-Induced Borehole Elongation: A Comparison Between the Four-Arm Dipmeter and the Borehole Televiewer in the Auburn Geothermal Well. *Journal of Geophysical Research*, 90(B7):5513–5521.

Reinecker, J., Heidbach, O., Tingay, M., Connolly, P., and Müeller, B. (2003). The 2004 release of the world stress map.

Sella, G. F. (2002). Revel: A model for Recent plate velocities from space geodesy. *Journal of Geophysical Research*, 107.

Sinha, B. K. and Kostek, S. (1996). Stress-induced azimuthal anisotropy in borehole flexural waves. *Geophysics*, 61(6):1899–1907.

Weber, J. C., Dixon, T. H., DeMets, C., Ambeh, W. B., Jansma, P., Mattioli, G., Saleh, J., Sella, G., Bilham, R., and Pérez, O. (2001). GPS estimate of relative motion between the Caribbean and South American plates, and geologic implications for Trinidad and Venezuela. *Geology*, 29:75–78.

Winkler, K. W. (1997). Acoustic evidence of mechanical damage surrounding stressed boreholes. *Geophysics*, 62(1):16–22.

Winkler, K. W., Sinha, B. K., and Plona, T. J. (1998). Effects of borehole stress concentrations on dipole anisotropy measurements. *Geophysics*, 63(1):11–17.

Zoback, M. D., Daniel, M., and Mastin, L. (1985). Well Bore Breakouts and In Situ Stress. *Journal of Geophysical Research*, 90(B7):5523–5530.

Zoback, M. D., Mastin, L., and Barton, C. (1986). In-Situ Stress Measurements in Deep Boreholes using Hydraulic Fracturing, Wellbore Breakouts, and Stoneley Wave Polarization. In *Proceedings of the International Symposium on Rock Stress and Rock Stress Measurements*, pages 289–299, Stockholm.

Zoback, M. D. and Zoback, M. L. (1989). Stress in the Earth's Lithosphere. In Fairbridge, R., editor, *Encyclopedia of Earth Sciences Series*, pages 1221–1232. Van Nostrand Reinhold Co., New York.

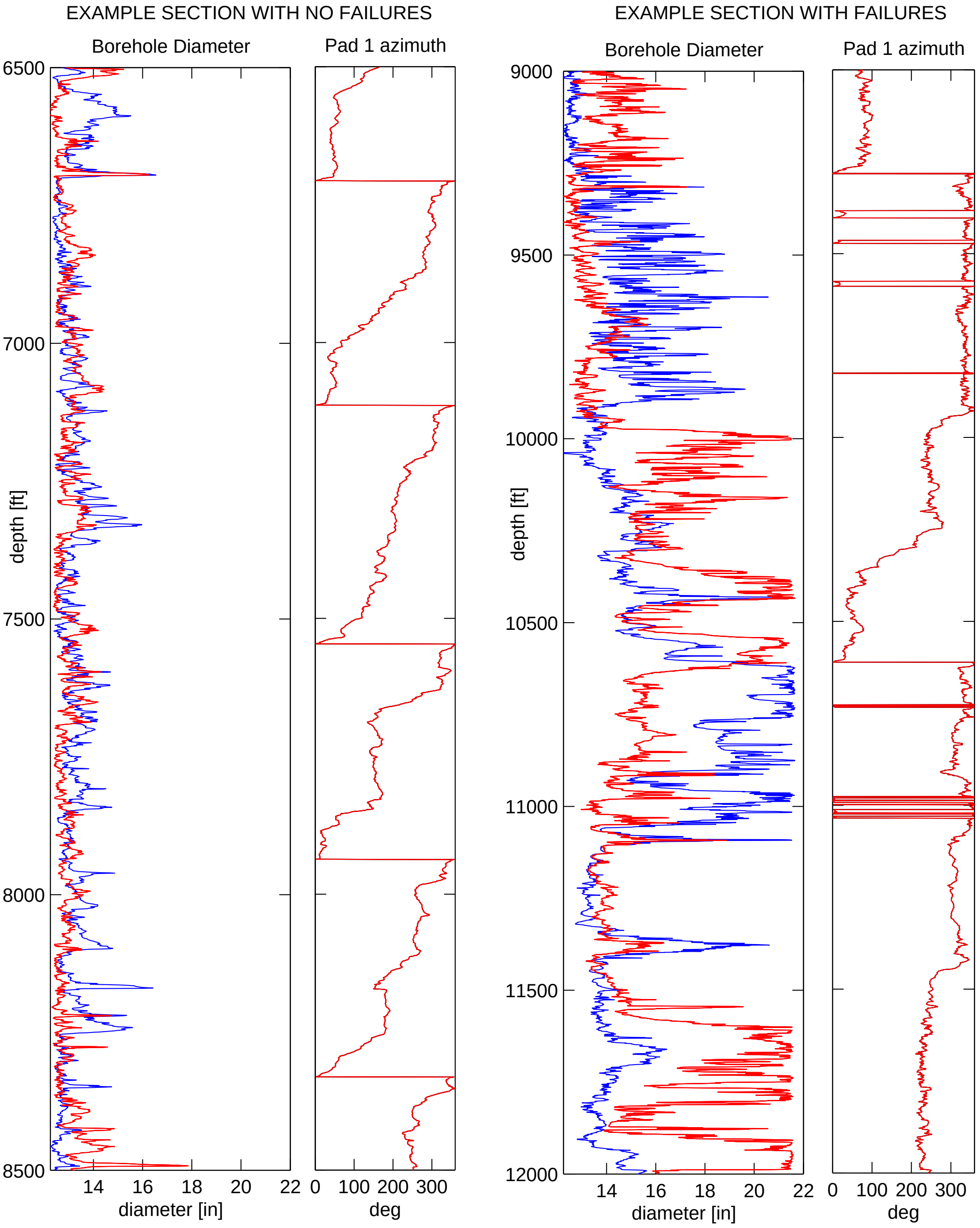

Figure 1: Four-arms caliper data in two depth intervals. On the left two panels, long and short borehole diameter and magnetic orientation of the dipmeter tool between 6500 and 8500 ft. On the right, data between 9000 and 12000 ft.

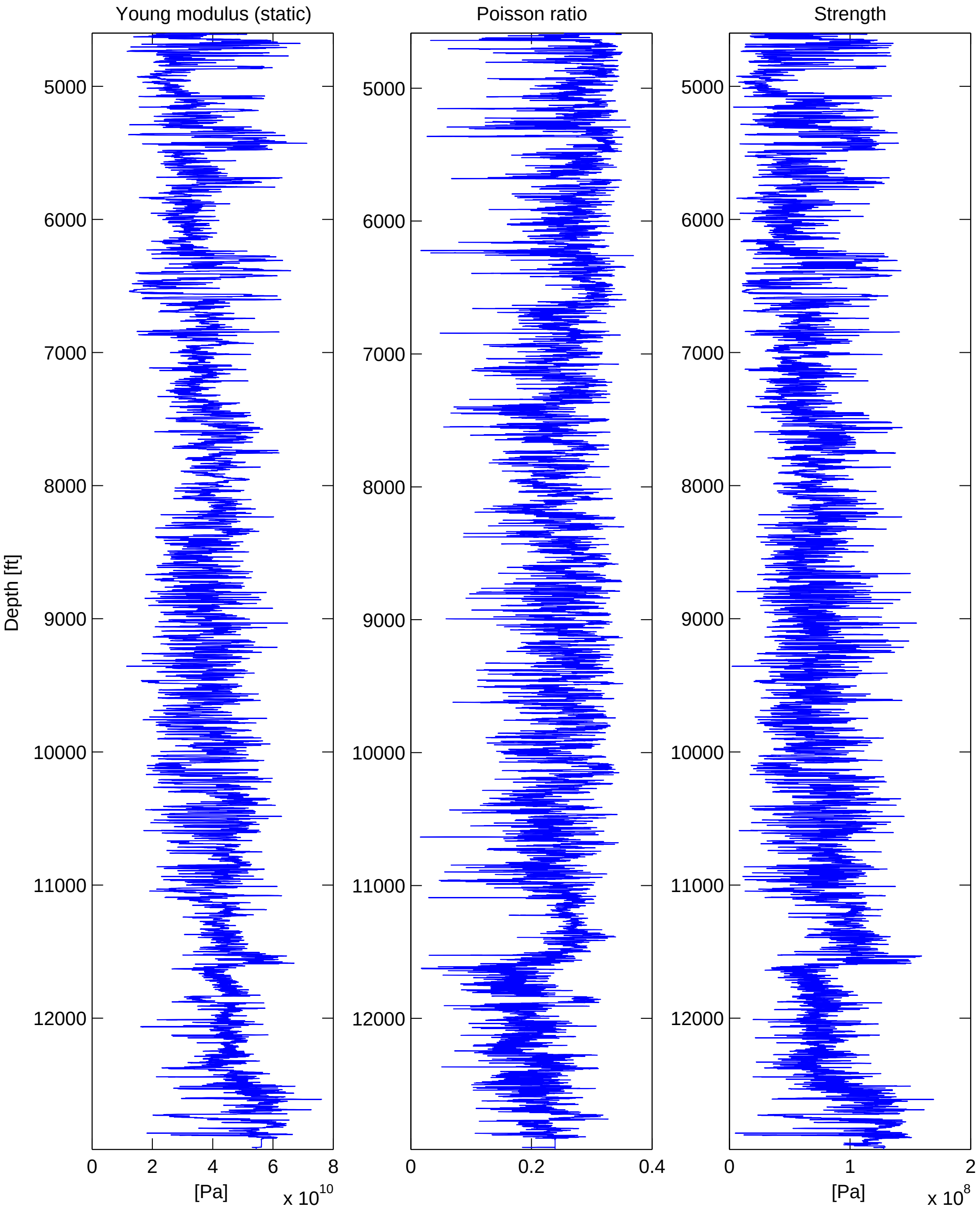

Figure 2: From left to right, Young's modulus, Poisson's ratio, and compressive rock strength with depth derived from log data.

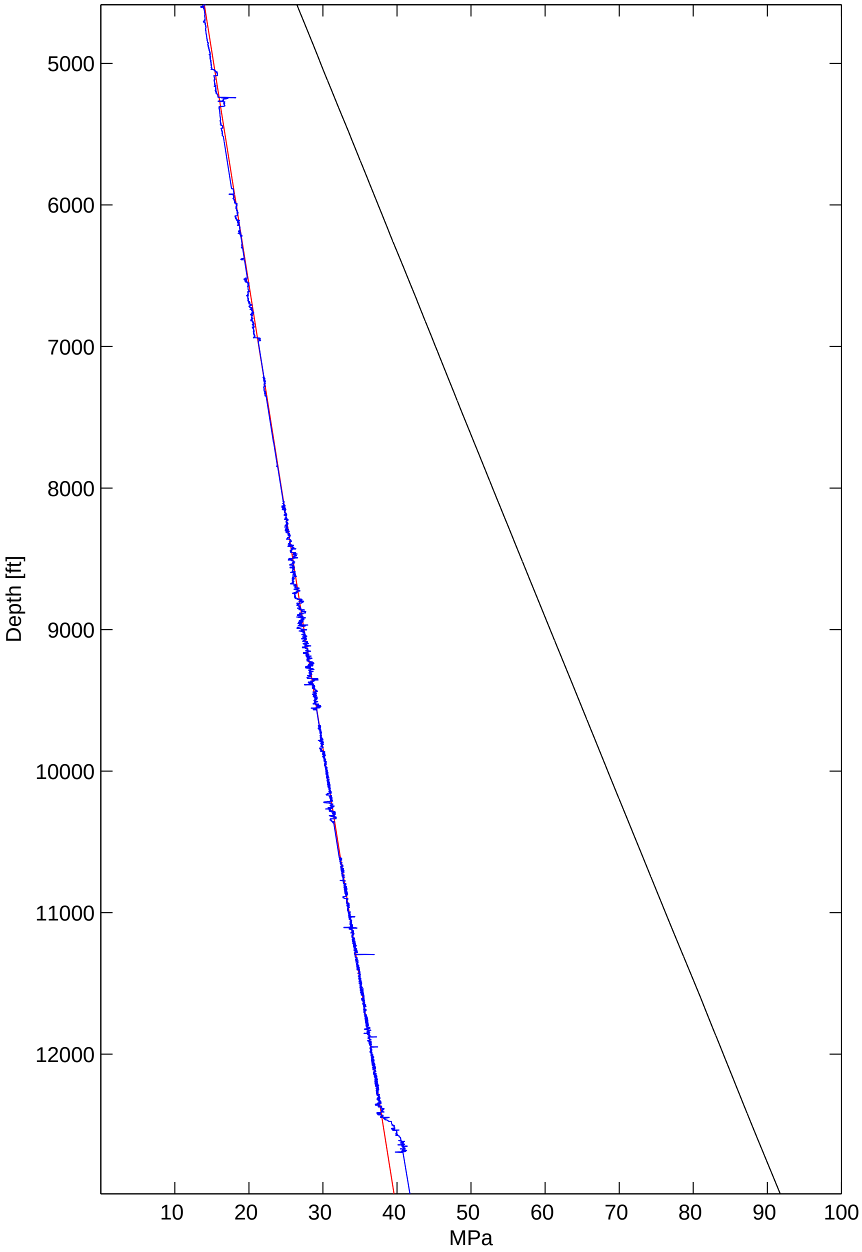

Figure 3: Vertical stress computed from overburden is plotted in black. Pore pressure assuming a hydrostatic gradient is shown in red, and drilling mud pressure corresponds to the blue curve.

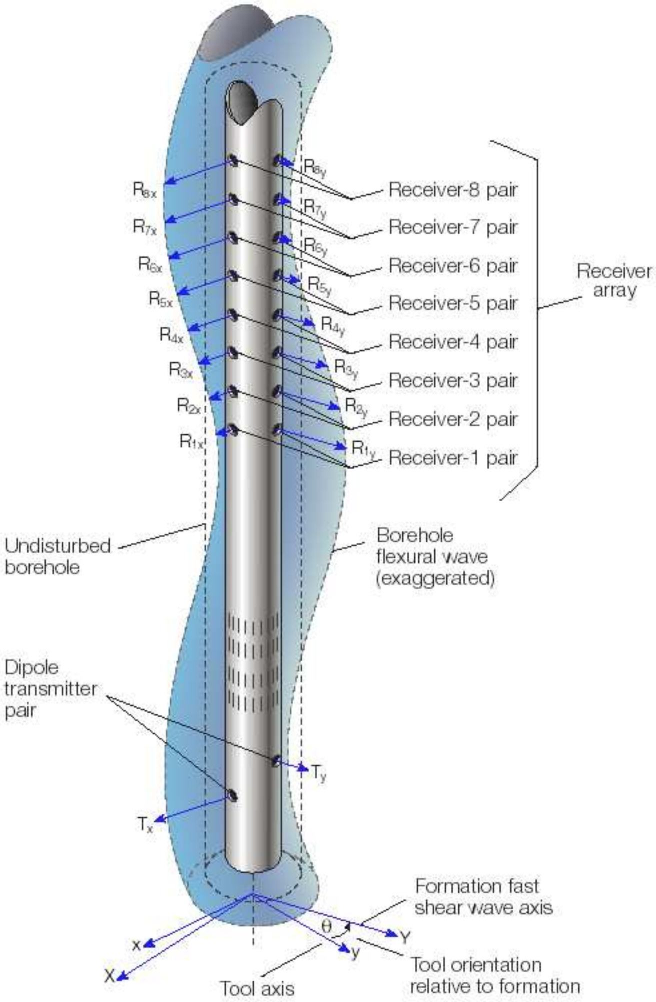

Figure 4: DSI tool diagrammatic configuration. Modified from Brie et al. (1998).

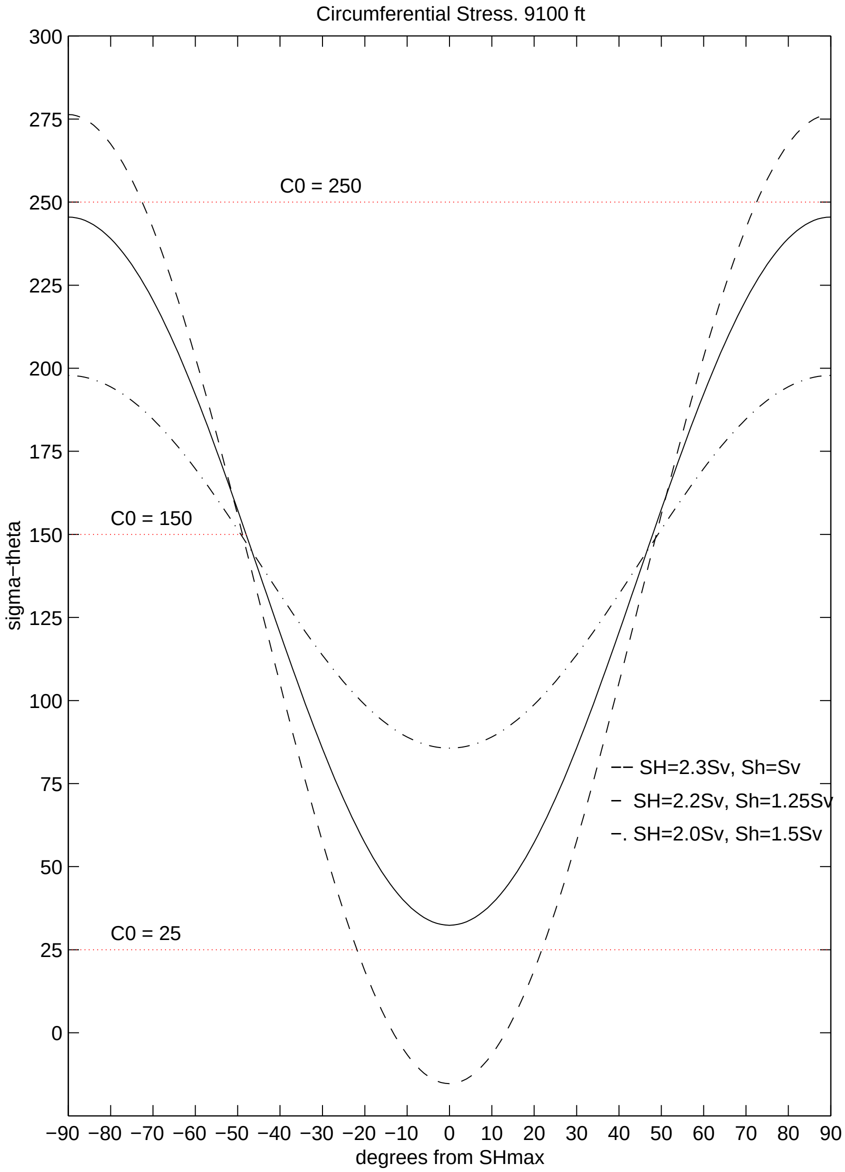

Figure 5: Hoop stress as a function of azimuth as described by equation 4 when $r = R$, $P_p = 27.8\ MPa$ and $\Delta P = -0.98\ MPa$. Three cases are shown and for all of them Sv is 56 MPa: (1) $SH = 2.3Sv$, $Sh = Sv$ (dashed line); (2) $SH = 2.2Sv$, $Sh = 1.25Sv$ (solid line); (3) $SH = 2.0Sv$, $Sh = 1.5Sv$ (dash-dotted line). When hoop stress exceeds the rock mechanical resistance at a particular angle, failures are expected. Because hoop stress is not constant everywhere around the hole, it is possible that failures are localized. In this example, when the rock strength is 250 MPa, failures only take place for case (1) and at azimuths -70° to -90° and 70° to 90°. When the rock strength is 150 MPa, failures are observed in all cases but still localized between -45° and -90° and 45-90°. For a strength of 25 MPa, failures occur at all azimuths for cases (2) and (3).

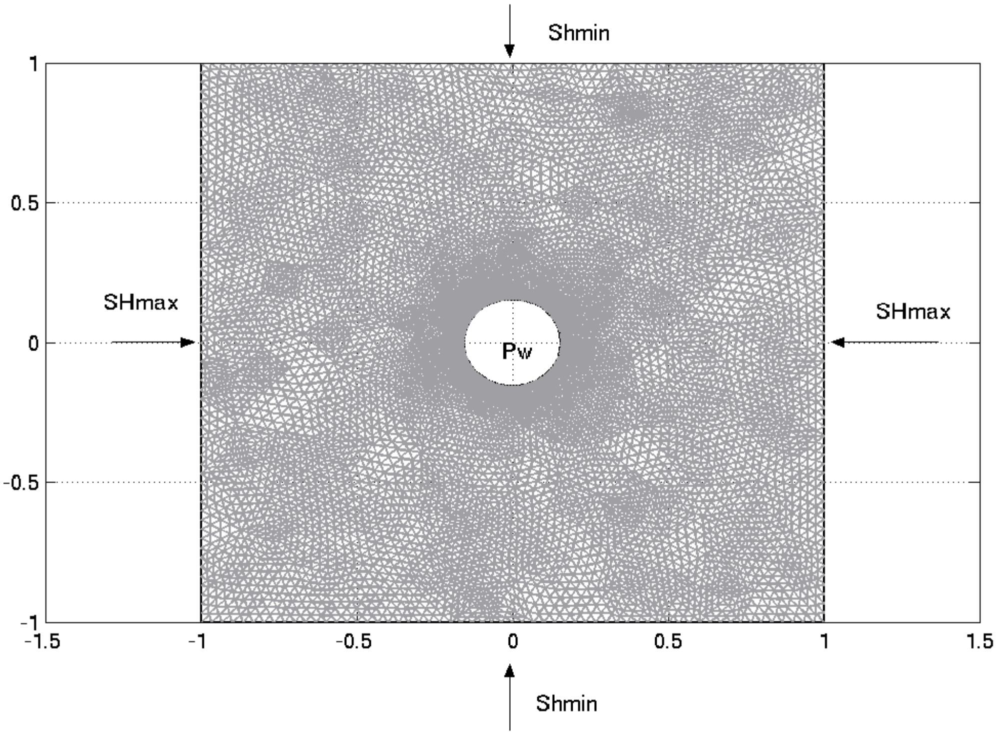

Figure 6: Model geometry, mesh, and boundary conditions. $SHmax$ is applied parallel to the x-direction. $Shmin$ is the boundary condition applied in the y-direction. P_w in the figure refers to mud pressure. Units in x and y are meters.

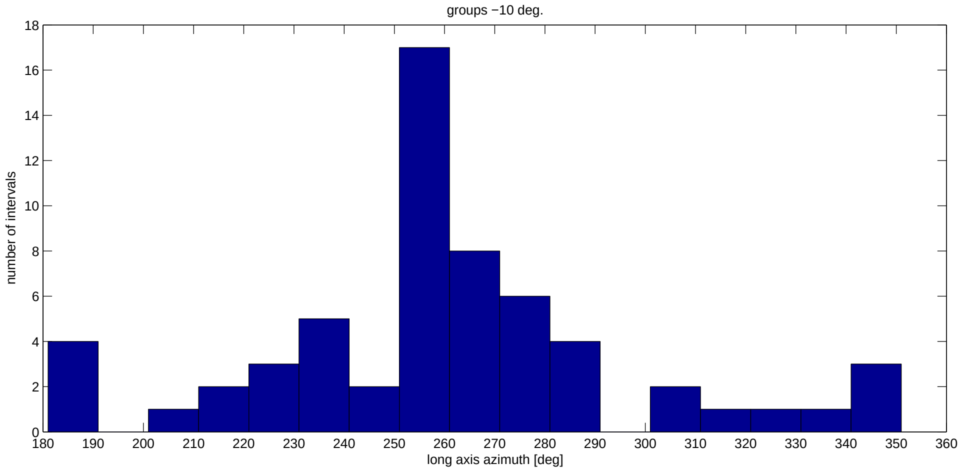

Figure 7: Histogram of $Shmin$ azimuths derived from breakouts orientations at different depths and throughout the well section.

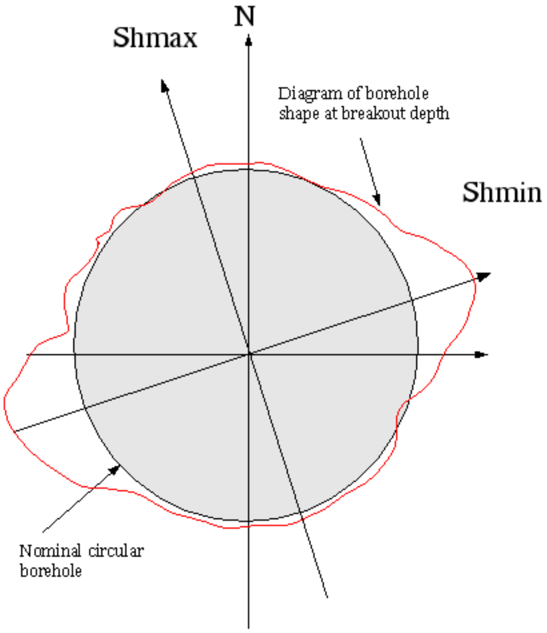

Figure 8: Diagrammatic representation of breakouts and stress orientation for the particular dataset. $SHmax$ is oriented NNW-SSE.

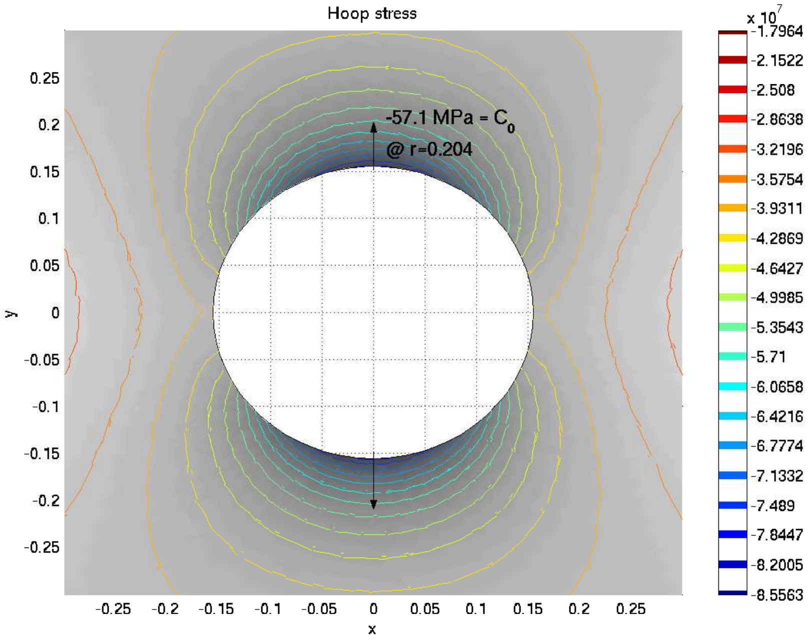

Figure 9: Model results. Contours represent hoop stress around the borehole. Formation properties for this model correspond to the data at 10120 ft. Hoop stress values similar to the compressive rock strength (-57.1 MPa) concentrate at approximately the borehole maximum radius observed at this breakout depth.

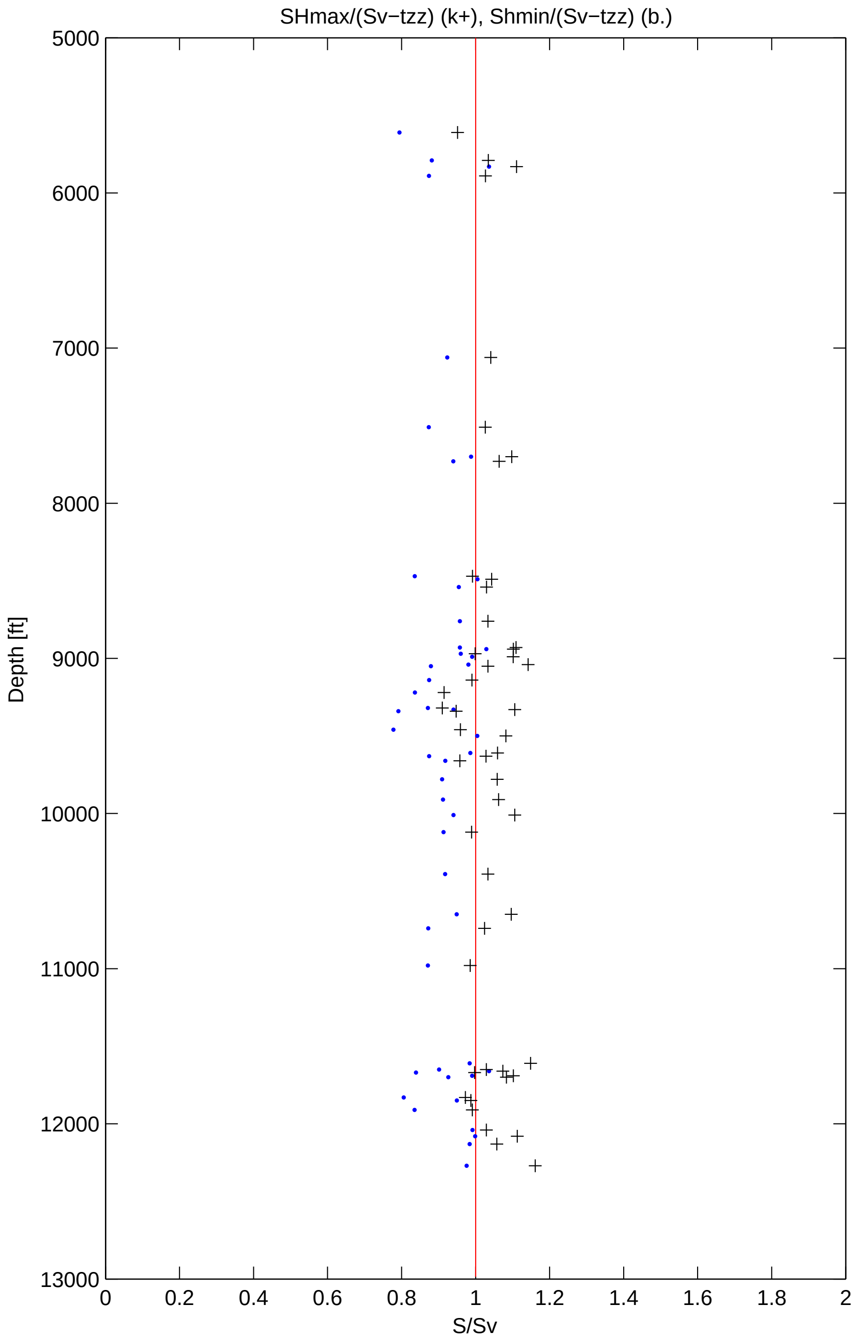

Figure 10: Maximum (black plus signs) and minimum (blue dots) horizontal stresses magnitudes relative to the vertical stress in depth. Data points are the results obtained from the stress modeling.

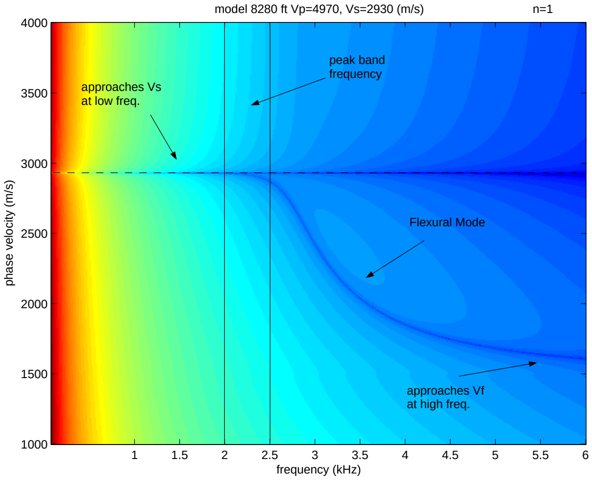

Figure 11: Roots of the period equation corresponding to azimuthal order 1 (flexural mode) in the phase velocity-frequency plane (code by Dr. Rama Rao at ERL, MIT). Shear wave velocity is 2930 m/s. Fluid velocity is 1500 m/s. The flexural wave asymptotes the S-wave velocity at low frequencies.

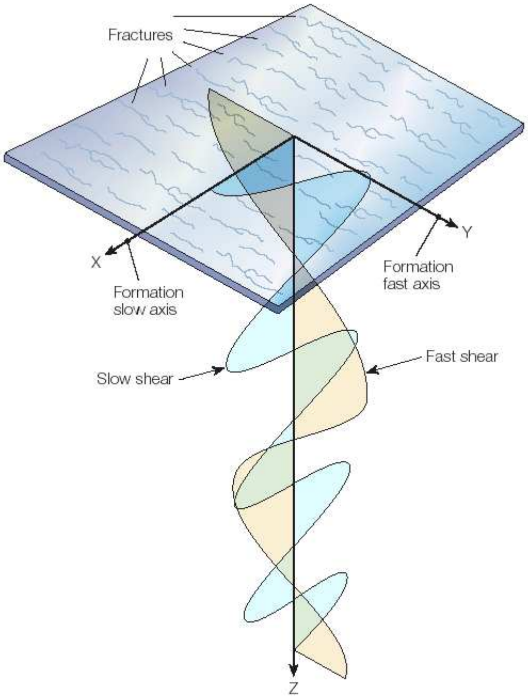

Figure 12: Diagram of shear wave splitting in an anisotropic formation. Modified from Brie et al. (1998). Waves propagate in the z-direction while particle displacements polarize in the horizontal plane. The slow shear direction is perpendicular to the orientation of fractures or similarly to the direction of the minimum horizontal stress.

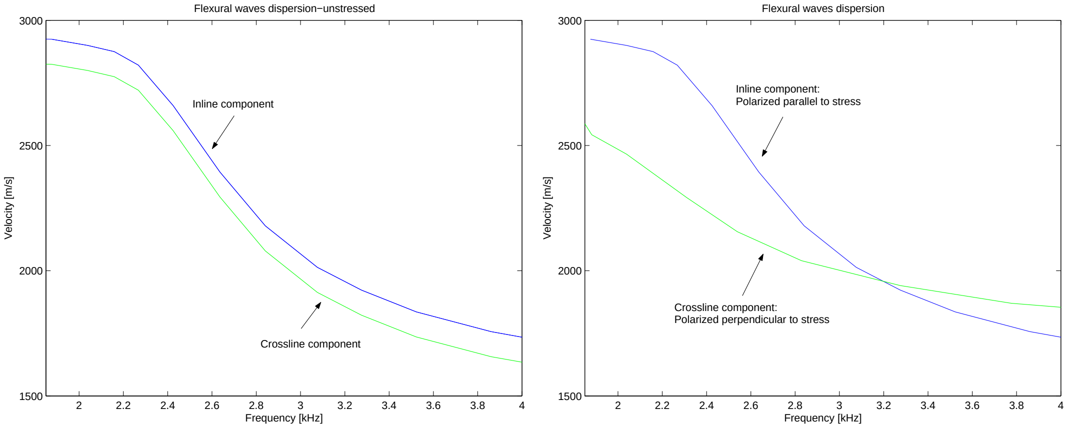

Figure 13: Dipole dispersion crossover. Figures are only descriptive. On the left, flexural dispersion curves as recorded from the inline and crossline components in a weakly anisotropic formation. On the right, corresponding response when an anisotropic stress field is superimposed. The shear-wave component polarized parallel to the maximum stress direction is the fastest at low frequencies. At high frequencies, hoop stresses are more compressive at 90° which is the polarization direction of the crossline component, thus becoming the fastest.

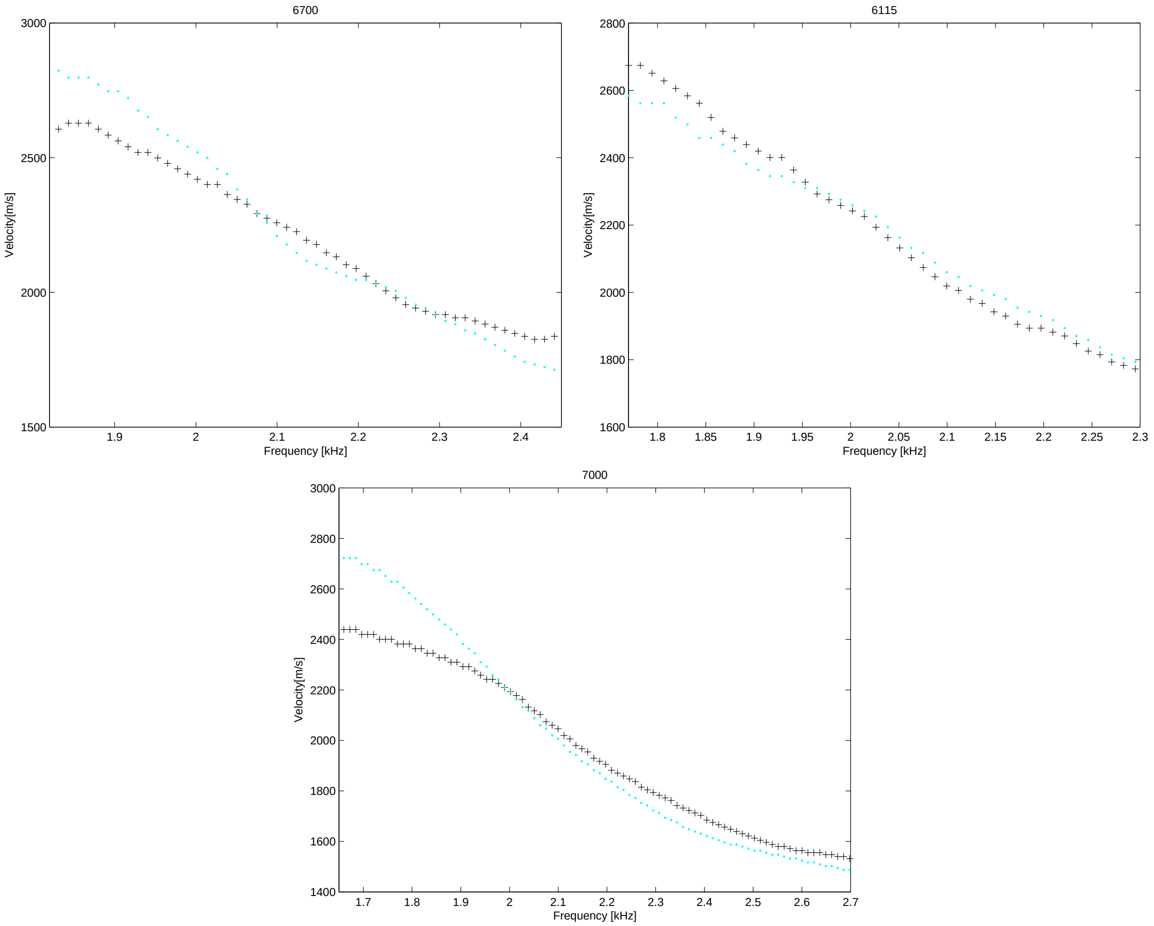

Figure 14: Example depths where crossovers are observed. Black plus signs represent inline components. Blue dots correspond to the crossline components. At the top left, data at 6700 ft. On the right, data at 6115 ft. At the bottom figure, dispersion curves from recordings at 7000 ft.

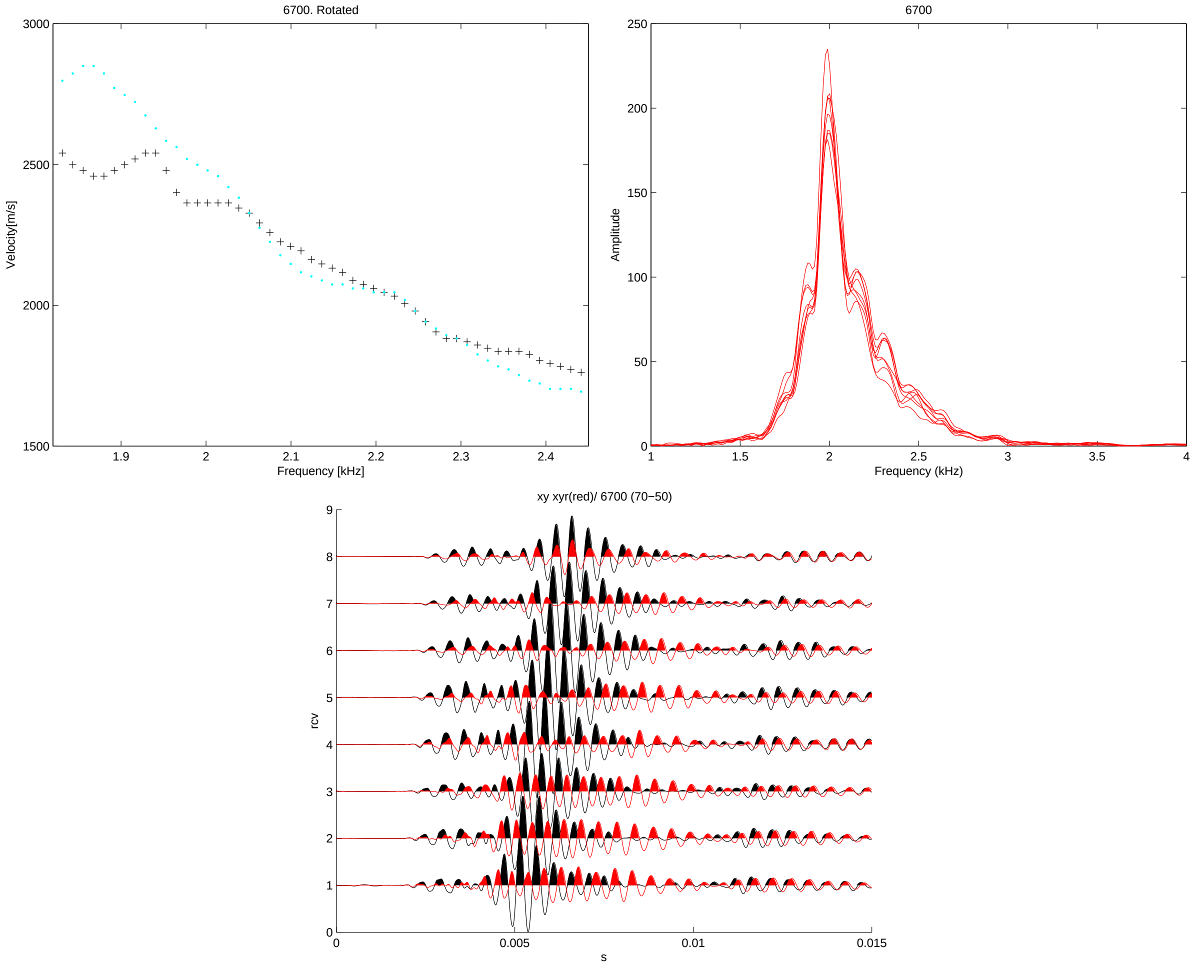

Figure 15: Processing results of frames at 6700 ft. The dispersion curves shown at the top left plot comes from the inline and crossline components rotated to principal axes of stress anisotropy. The effectiveness of the rotation can be verified in the lower plot where the cross-components xy are plotted before (black) and after rotation (red). Energy of the flexural wave is minimized in all receiver signals.

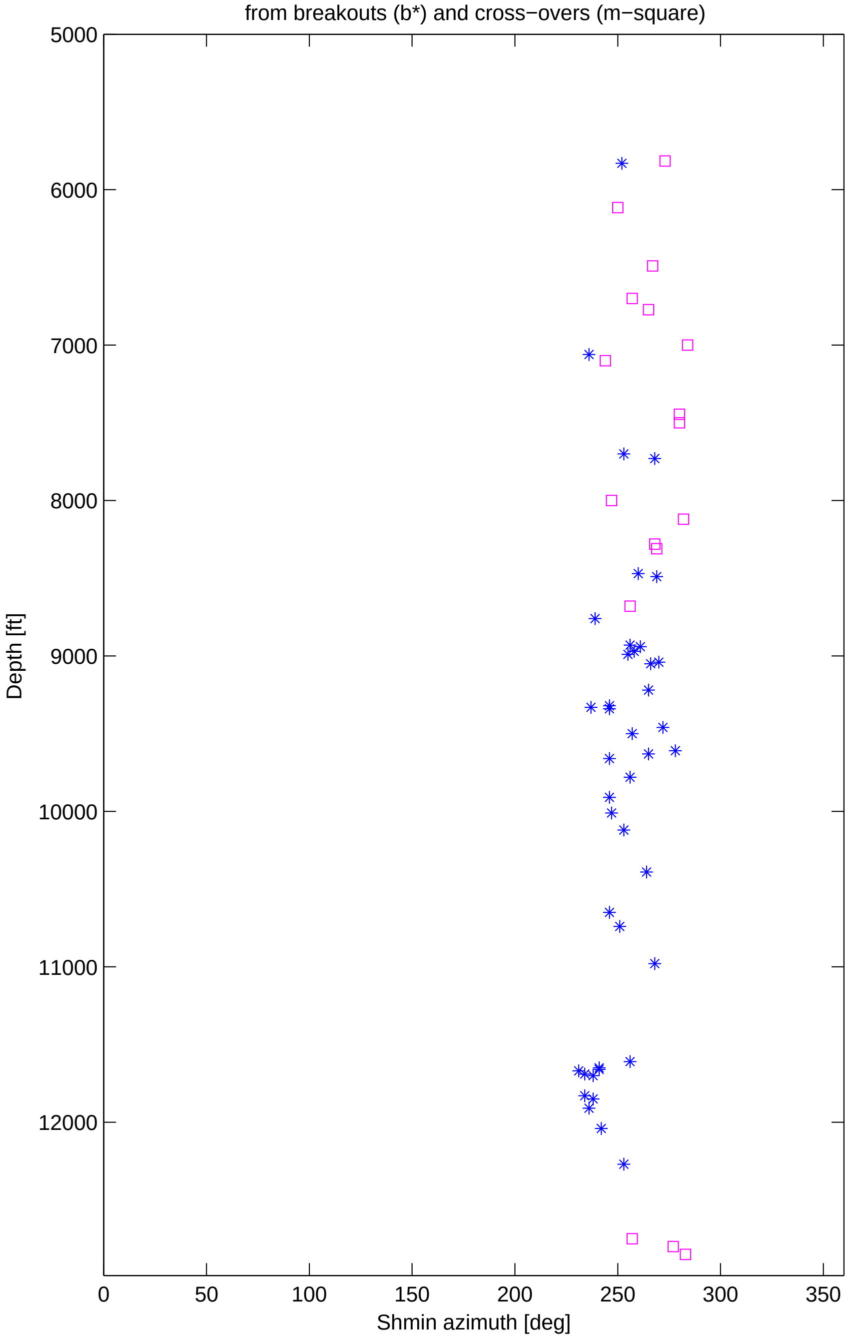

Figure 16: *Shmin* azimuths obtained from cross-dipole data rotation (magenta squares). The orientations computed from breakouts are also displayed (blue stars). *Shmin* direction is well constrained from these two measurements to be around 260°, giving a dominant strike E10N-W10S.

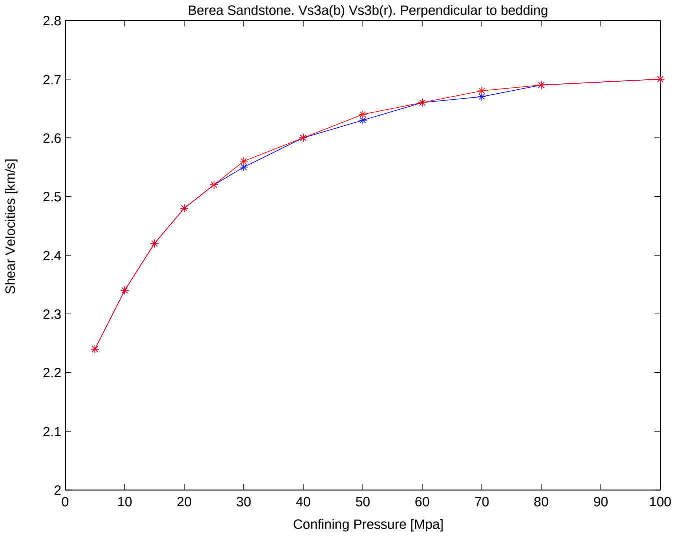

Figure 17: Shear wave velocities with increasing confining pressures measured perpendicular to bedding planes in Berea sandstone at two orthogonal transducers. Data from Lo et al. (1986).

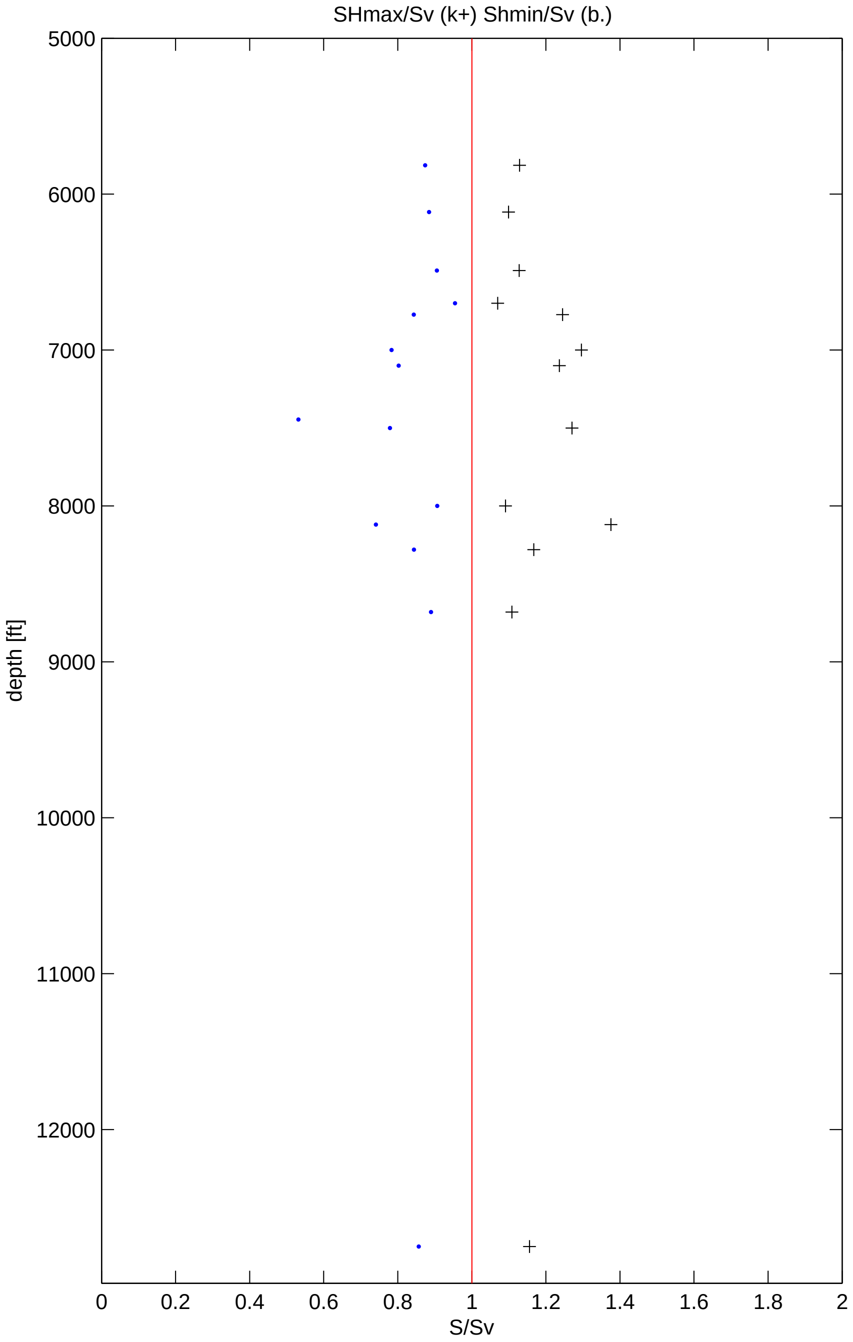

Figure 18: Ratios of maximum (black plus signs) and minimum (blue dots) stress to vertical stress estimated from stress-induced velocity anisotropies at crossover depths. Experimental data used as base of comparisons are elastic velocities of Berea sandstone reported in Lo et al. (1986).

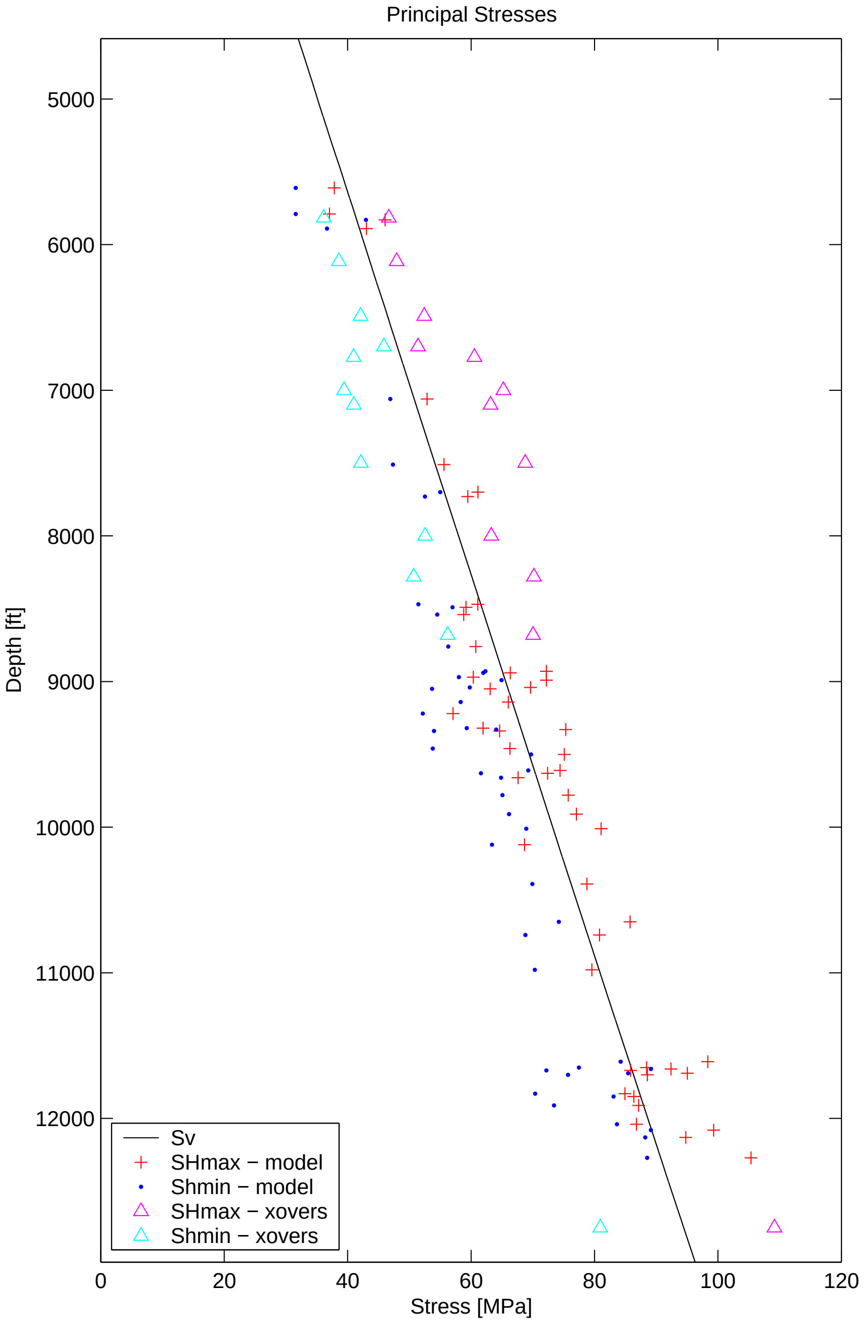

Figure 19: Principal stresses magnitudes vs. depth. Vertical stress is plotted in black. Horizontal stresses derived from the elastic model are shown in red plus signs (maximum) and blue dots (minimum). Equivalent results from shear velocity anisotropy are plotted with triangles.

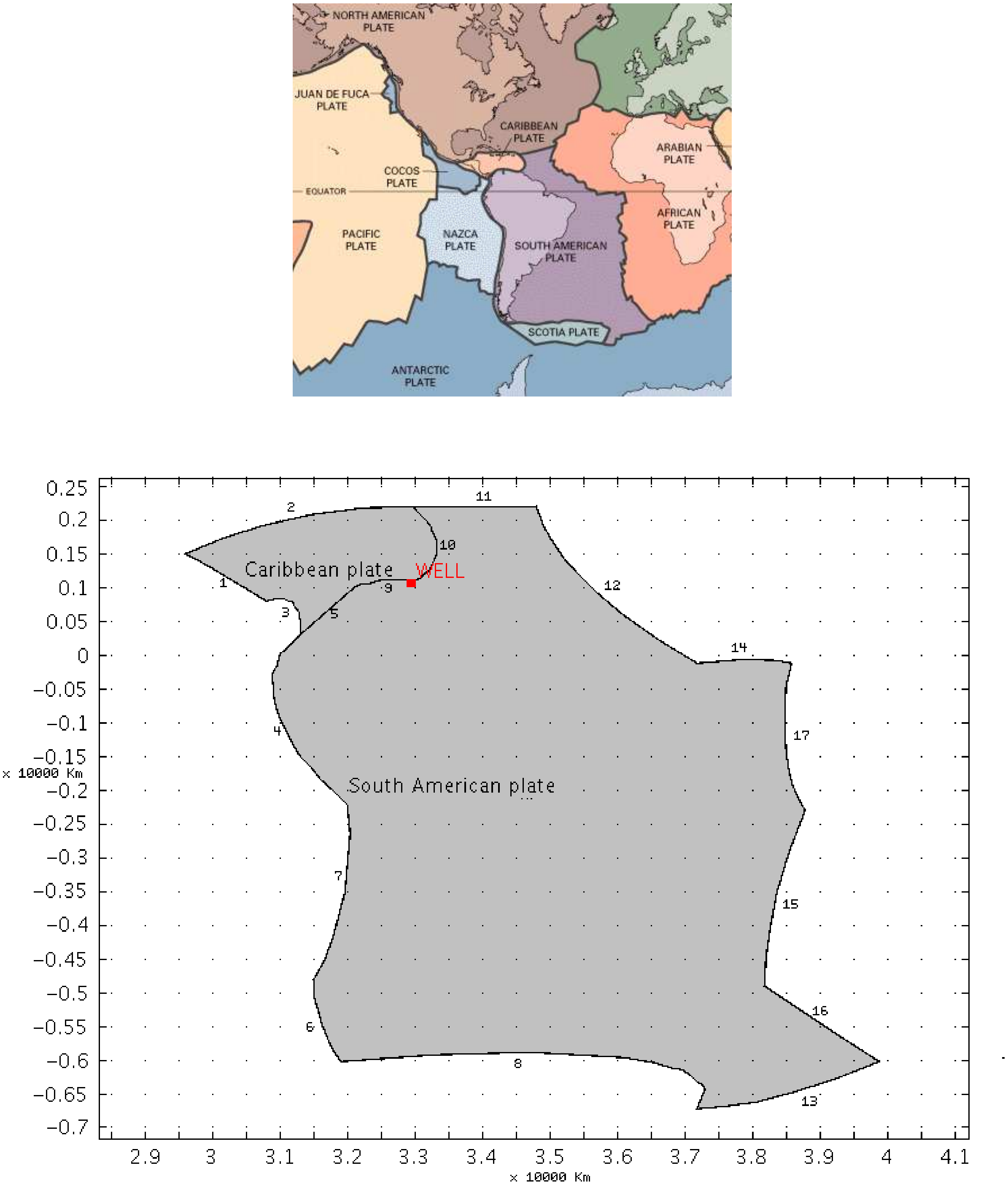

Figure 20: Geometry of the regional stress model. The model is a 2D (map view) representation of the Caribbean and South America plates. The well location and the numbering of the model boundaries are indicated.

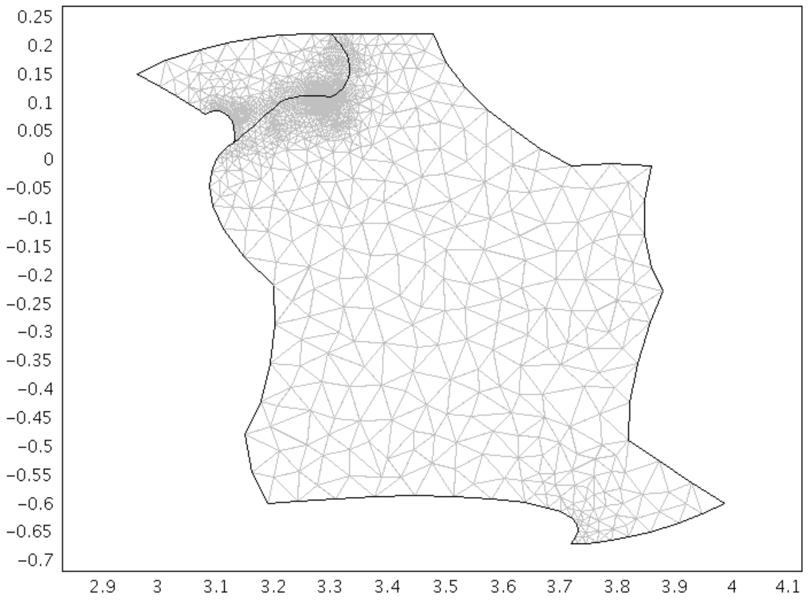

Figure 21: Finite element mesh of the regional stress model.

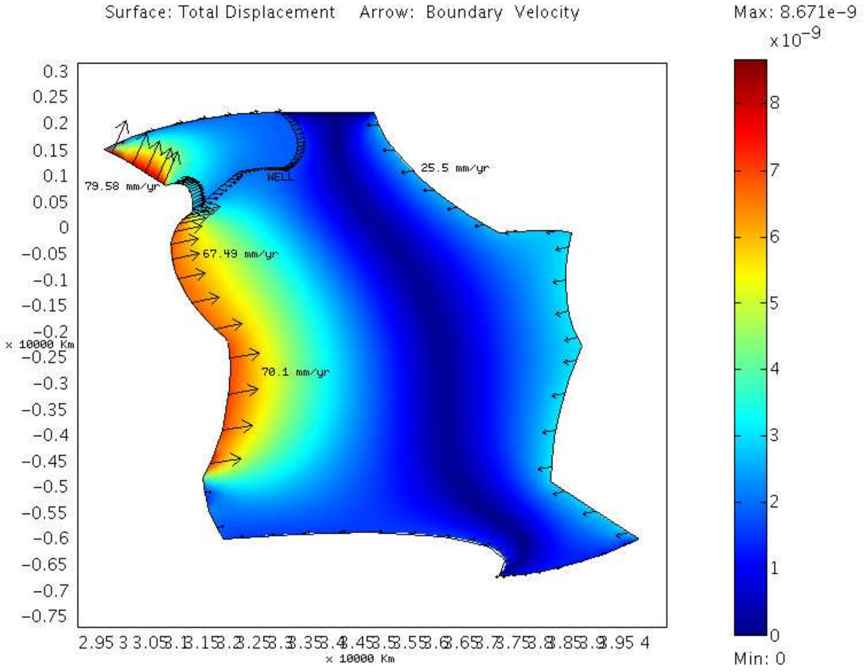

Figure 22: Boundary conditions corresponding to velocities from the global model REVEL. Arrows' length is proportional to velocity magnitude at the plate boundary location. The surface plot shows total displacement. Units are 10^{10} *mm*.

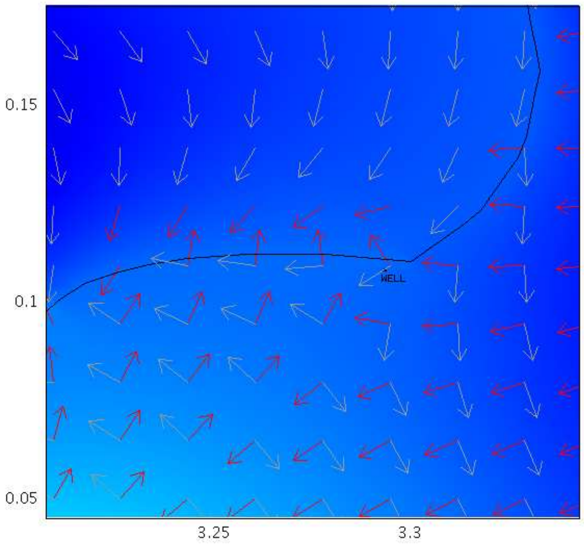

Figure 23: Principal stresses direction around the well location for REVEL velocities imposed at the model boundaries. Red arrows represent maximum horizontal stress. Minimum stress orientation is indicated in gray.

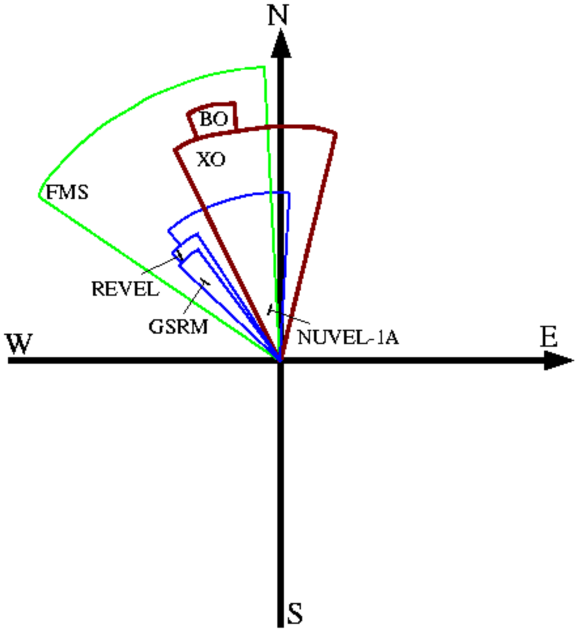

Figure 24: *SHmax* direction. Breakout data (BO) indicate that *SHmax* azimuth is in the range 340-350°. *SHmax* azimuth obtained from crossovers (XO) is between 334 and 14°. Maximum stress orientation according to the regional stress models are indicated in blue. The western limit of the three models correspond to results when Nazca's velocity is reduced in 50%. NUVEL-1A, REVEL and GSRM velocities give *SHmax* azimuth ranges of 319-2.5°, 315-327° and 314-324° respectively. In green, a range of possible *SHmax* azimuths obtained from focal mechanisms (FMS) in the World Stress Map (304-357°).